



The Effect of Dust Evolution and Traps on Inner Disk Water Enrichment

Anusha Kalyaan¹ , Paola Pinilla² , Sebastiaan Krijt³ , Andrea Banzatti⁴ , Giovanni Rosotti⁵ , Gijs D. Mulders^{6,7} ,
Michiel Lambrechts⁸ , Feng Long^{9,12} , and Gregory J. Herczeg^{10,11}

¹ Department of Physics, Texas State University, 749 N Comanche St, San Marcos, TX 78666, USA; a_k363@txstate.edu

² Mullard Space Science Laboratory, University College London, Holmbury St Mary, Dorking, Surrey RH5 6NT, UK

³ School of Physics and Astronomy, University of Exeter, Stocker Road, Exeter EX4 4QL, UK

⁴ Department of Physics, Texas State University, 749 N Comanche St, San Marcos, TX 78666, USA

⁵ Dipartimento di Fisica, Università degli Studi di Milano, via Giovanni Celoria 16, I-20133 Milano, Italy

⁶ Facultad de Ingeniería y Ciencias, Universidad Adolfo Ibáñez, Av. Diagonal las Torres 2640, Peñalolén, Santiago, Chile

⁷ Millennium Institute for Astrophysics, Chile

⁸ Center for Star and Planet Formation, GLOBE Institute, University of Copenhagen, Øster Voldgade 5-7, DK-1350 Copenhagen, Denmark

⁹ Lunar and Planetary Laboratory, University of Arizona, Tucson, AZ 85721, USA

¹⁰ Kavli Institute for Astronomy and Astrophysics, Peking University, Beijing 100871, People's Republic of China

¹¹ Department of Astronomy, Peking University, Beijing 100871, People's Republic of China

Received 2023 May 5; revised 2023 June 7; accepted 2023 July 1; published 2023 August 23

Abstract

Substructures in protoplanetary disks can act as dust traps that shape the radial distribution of pebbles. By blocking the passage of pebbles, the presence of gaps in disks may have a profound effect on pebble delivery into the inner disk, crucial for the formation of inner planets via pebble accretion. This process can also affect the delivery of volatiles (such as H₂O) and their abundance within the water snow line region (within a few au). In this study, we aim to understand what effect the presence of gaps in the outer gas disk may have on water vapor enrichment in the inner disk. Building on previous work, we employ a volatile-inclusive disk evolution model that considers an evolving ice-bearing drifting dust population, sensitive to dust traps, which loses its icy content to sublimation upon reaching the snow line. We find that the vapor abundance in the inner disk is strongly affected by the fragmentation velocity (v_f) and turbulence, which control how intense vapor enrichment from pebble delivery is, if present, and how long it may last. Generally, for disks with low to moderate turbulence ($\alpha \leq 1 \times 10^{-3}$) and a range of v_f , radial locations and gap depths (especially those of the innermost gaps) can significantly alter enrichment. Shallow inner gaps may continuously leak material from beyond it, despite the presence of additional deep outer gaps. We finally find that for realistic v_f ($\leq 10 \text{ m s}^{-1}$), the presence of gaps is more important than planetesimal formation beyond the snow line in regulating pebble and volatile delivery into the inner disk.

Unified Astronomy Thesaurus concepts: [Protoplanetary disks \(1300\)](#); [Planet formation \(1241\)](#)

1. Introduction

Millimeter interferometric observations reveal that protoplanetary disks often exhibit substructure in dust emission in the form of gaps and rings (e.g., Huang et al. 2018; Long et al. 2018; Andrews 2020), and more recently, even in gas (Teague et al. 2018; Zhang et al. 2021; Wölfer et al. 2023). Gaps, potentially carved by the presence of planetary companions (Paardekooper & Mellema 2006; Rice et al. 2006; Zhu et al. 2012; Marzari et al. 2019; Marzari & D'Angelo 2020), play an important role in shaping the dust distribution and dynamics in disks by slowing the radially inward drift of dust particles and concentrating them in pressure bumps beyond gaps (Pinilla et al. 2012), becoming observable ring-like structures in disks.

Dust trapping in rings beyond gaps, however, has consequences beyond the local disk region. By halting dust delivery, the presence of gaps in outer disk regions can create expansive solid reservoirs in the outer disk, leading to large

observed dust disks with sizes spanning hundreds of au. In contrast, the rapid radial drift of dust in smooth unstructured disks likely make them compact, radially extending to only ~tens of au (Huang et al. 2018; Long et al. 2018, 2019; Appellgren et al. 2020; Toci et al. 2021; van der Marel & Mulders 2021). Moreover, the trapping of dust and pebbles in the outer disk can significantly impact planet formation and chemistry in the inner disk. Pebble mass fluxes into the inner few au can dictate what types of planets can form via pebble accretion there, whether they may be Earths, super-Earths, or even the cores of giant planets (Lambrechts et al. 2019). Additionally, these incoming pebbles and dust particles carry significant masses of volatile ices (such as H₂O and CO) within them (Pontoppidan et al. 2014). The presence of any gaps and traps that halt their passage from the outer to the inner disk therefore not only curtail the formation of larger planets in the terrestrial planet region, it can also reduce the overall mass of volatiles brought into the inner disk, where they may sublimate into vapor within the snow line region, affecting the local chemistry, the amount of volatiles that is accreted into forming planetesimals, and even the atmospheric compositions of forming planets (Ciesla & Cuzzi 2006; Morbidelli et al. 2016; Booth et al. 2017; Venturini et al. 2020; Schneider & Bitsch 2021a, 2021b; Öberg & Bergin 2021). Inner disk volatile abundances can also provide a novel way to constrain

¹² NASA Hubble Fellowship Program Sagan Fellow.

pebble mass fluxes into the terrestrial planet formation region (Banzatti et al. 2020; Kalyaan et al. 2021).

To get a broader and more complete view of the delivery of ice-rich pebbles from the outer to the inner disk, it is critical to look beyond millimeter interferometry that informs us about the presence of gaps in the outer disk and radial drift there, and consider infrared spectra of molecules that inhabit the warm inner regions. Synthesizing insights from both types of observations, Banzatti et al. (2020) found an anticorrelation between disk size (and the presence of substructure) and the water luminosity tracing the abundance of the water molecules in the inner disk. They found that smaller disks generally show higher H₂O luminosities (suggestive of higher H₂O column densities) than larger disks with substructure, indicating that pebble delivery regulated by the presence of gaps in the outer disk may be able to affect the inner disk vapor abundance significantly. This scenario was then modeled and verified with a volatile-inclusive disk evolution model in Kalyaan et al. (2021), where the effect of a gap on inner disk vapor enrichment was explored. Kalyaan et al. (2021) modeled a radially drifting, ice-bearing, single-sized dust population that lost ice to sublimation on approaching the water snow line in the inner disk. This work found that in general, inner disk water vapor abundance evolved with time. As pebbles rich in water ice drifted inwards into the inner disk, the vapor mass increased, and peaked when the bulk of the icy pebble population was brought inward, and later declined with time as water vapor was accreted onto the star. They also found that the presence of a gap and its radial location significantly influenced the inner disk vapor enrichment, with deep innermost gaps (outside of the snow line) drastically restricting the delivery of ice-rich pebbles into the inner disk.

In this work, we build on our previous modeling by incorporating a “full” evolving dust population (shaped by growth and fragmentation) via the two-population model by Birnstiel et al. (2012), rather than the single-sized dust population previously assumed. Previous studies have also used the two-population model or similar models to model the snow line region and volatile/ice transport and distribution in the disk. Schoonenberg & Ormel (2017) used a characteristic particle method with an assumed particle size at each radius and time to explore whether a complex internal aggregate structure of drifting icy pebbles could foster planetesimal formation just inside and outside of the snow line. Similarly, Drażkowska & Alibert (2017) use the two-population model within a full disk evolution model to find that planetesimal formation is favored just beyond the snow line. Finally, Booth et al. (2017) and Schneider & Bitsch (2021a, 2021b) also used this model to explore the influence of pebble growth and drift on the chemical enrichment of inner disk gas and giant planet atmospheres. While the above studies collectively include detailed microphysics as well as planet formation and migration, to our knowledge, no study so far has systematically explored the effect of disk gaps, including their location and depth, on vapor enrichment in the inner disk with an evolving dust population model, as we present here.

In this study, we perform detailed parameter studies on various disk and vapor/particle properties such as turbulent viscosity α , the diffusivities of vapor and dust, and the fragmentation velocities of ice and silicate particles; gap properties such as their radial location and depth; and study the effect of each property on inner disk vapor enrichment.

Moreover, we also consider new insights from very recent experiments performed at lower temperatures (more consistent with the outer solar nebula) that suggest that the fragmentation velocities of icy silicates and pure silicates may be comparable to each other, i.e., $\sim 1 \text{ m s}^{-1}$ (Gundlach et al. 2018; Musiolik & Wurm 2019), rather than what was suggested from older experiments (Blum & Wurm 2000; Gundlach & Blum 2015; Musiolik et al. 2016) that icy particles were likely to be more stickier by at least an order of magnitude. We finally also study the effect of including planetesimal formation on vapor content in the inner disk.

This paper is organized as follows. We describe the model used in this work in Section 2 and delve into the results of our detailed parameter study in Section 3. We discuss in detail the main insights gained from this work in Section 4 and present the main conclusions of our study in Section 5.

2. Methods

The main motivation of this work is to model pebble dynamics in disks with gaps and assess the effect of structure on icy pebble delivery into the inner disk and the resulting vapor enrichment there. We use the multimillion-year disk evolution model with volatile transport as described in Kalyaan & Desch (2019), supplemented by the addition of structure in the form of gaps as described in Kalyaan et al. (2021). We then incorporate the two-population model from Birnstiel et al. (2012) to include a “full” dust population, with particle size at each location evolving through growth and fragmentation, and then finally also include planetesimal formation by using clumping criteria from recent streaming instability simulations (see Figure 1). In this section, we will describe the specific additions we have made here over the model described in Kalyaan et al. (2021). We list all the model parameters used in Table 1.

2.1. Gas Transport

We evolve a disk of mass $0.05 M_{\odot}$ around a solar-mass star with the standard evolution equations from Lynden-Bell & Pringle (1974), evolving the surface density Σ over a discretized model grid of 450 radial zones between 0.1 to 500 au as follows:

$$\frac{\partial \Sigma}{\partial t} = \frac{1}{2\pi r} \frac{\partial \dot{M}}{\partial r}, \quad (1)$$

where the rate of mass flow \dot{M} is given as

$$\dot{M} = 6\pi r^{1/2} \frac{\partial}{\partial r} (r^{1/2} \Sigma \nu). \quad (2)$$

The initial gas surface density $\Sigma(r)$ is equivalent to a power law with an exponential taper in the outer disk (Hartmann et al. 1998) as

$$\Sigma = \Sigma_0 \left(\frac{r}{r_0} \right)^{-1} \exp \left[-\frac{r}{r_0} \right] \text{ g cm}^{-3}. \quad (3)$$

Here, $\Sigma_0 = 14.3 \text{ g cm}^{-3}$ at the characteristic radius $r_0 = 70 \text{ au}$. Note that even though initial disk size is 500 au in our models, most of the disk mass is concentrated within r_0 . We assume the turbulent viscosity ν of the disk follows the standard prescription $\nu = \alpha c_s^2 / \Omega$, where c_s is the local sound speed and Ω is the Keplerian angular frequency. We assume a typical $\alpha = 10^{-3}$ throughout the disk (unless stated otherwise). As done previously in Kalyaan & Desch (2019), we also

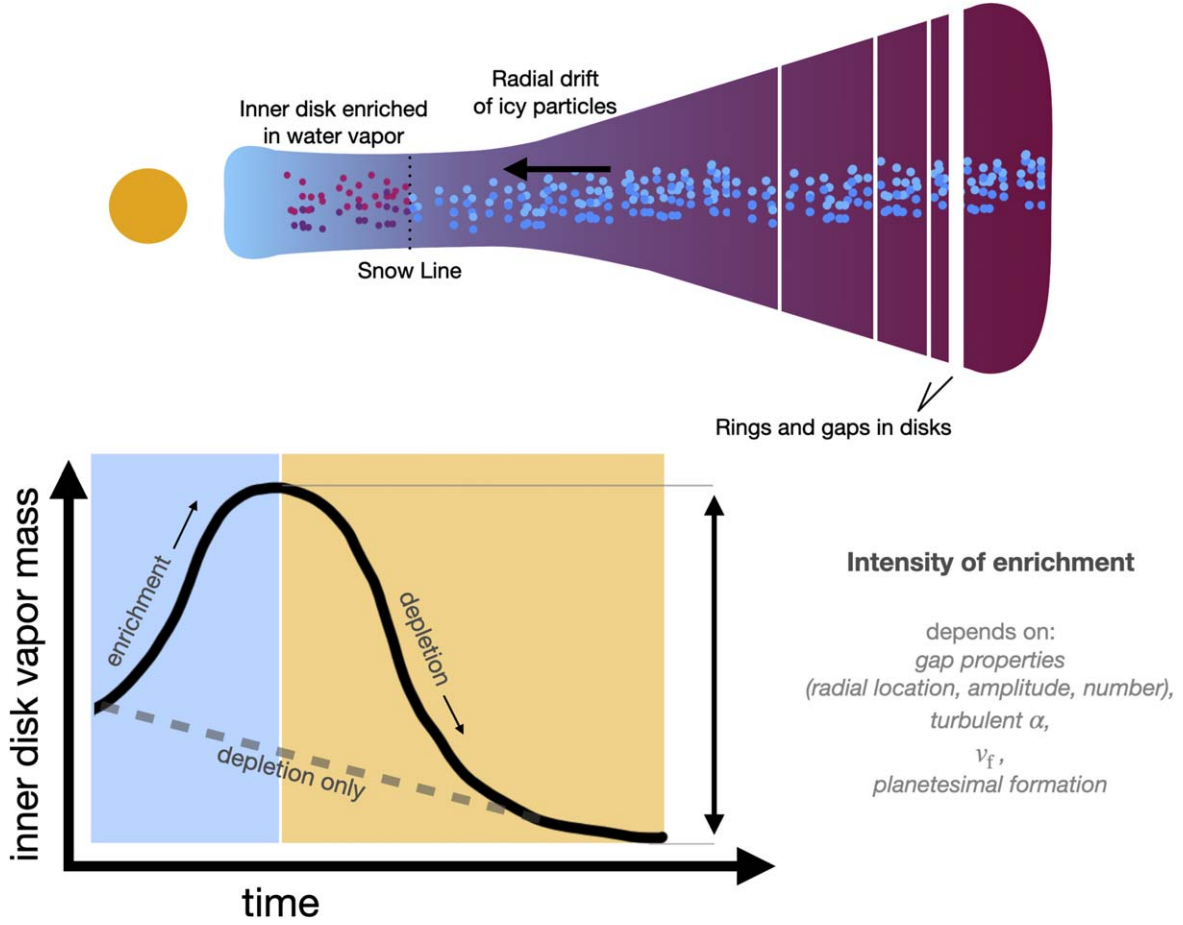


Figure 1. Schematic figure presenting our multimillion-year volatile-inclusive disk evolution model with disk structure (top). Icy particles radially drift inward, enriching the inner disk with water vapor. The vapor mass typically rises with incoming pebble drift, peaks, and then declines with time as disk mass accretes onto the star (bottom).

assume that the disk is heated both by stellar radiation and accretion heating, and denote the contribution of each as T_{acc} for accretional heating, and T_{pass} for passive starlight, combined as follows:

$$T(r) = [T_{\text{acc}}(r)^4 + T_{\text{pass}}(r)^4]^{1/4}, \quad (4)$$

where r is the radial distance from the star. Here, T_{acc} is given by

$$T_{\text{acc}}(r) = \left[\frac{27}{128} \frac{k}{\mu\sigma} \Sigma(r)^2 \kappa \alpha \Omega(r) \right]^{1/3}, \quad (5)$$

where $\Sigma(r)$, is the gas surface density in the disk, $\Omega(r)$ is the Keplerian angular frequency, k is the Boltzmann constant, σ is the Stephen–Boltzmann’s constant, μ is the mean molecular weight of the bulk gas, and κ is the fine dust opacity, assumed to be $5 \text{ cm}^2 \text{ g}^{-1}$. For accretion heating, the constant fiducial α is adopted throughout the disk (including within the gap, as we explain in detail below).

As we did before in Kalyaan et al. (2021), we assume T_{pass} to be

$$T_{\text{pass}}(r) = 118 \left(\frac{r}{1 \text{ au}} \right)^{-0.5} \text{ K}. \quad (6)$$

We also do not allow the temperature to exceed 1400 K (\approx silicate vaporization limit) in the innermost disk. We

additionally impose a minimum temperature = 7 K in the outermost colder regions. We run all our simulations for 5 Myr.

2.1.1. Gap Formation

As we did previously in Kalyaan et al. (2021), instead of directly modeling the formation of a planet carving a gap in the gaseous disk best done in 2D/3D, we incorporate instantaneous gap formation at $t=0$ (start of simulation) by implementing a Gaussian peak in the turbulent viscosity α profile as below:

$$\alpha(r) = \alpha_0 + (\alpha_{\text{gap}} - \alpha_0) \exp(-x^2). \quad (7)$$

Here, α_0 is the uniform turbulent viscosity α chosen throughout the disk, and α_{gap} is the peak value of α imposed at the center of the gap, which creates a gap in the disk by depleting the gas surface density here. $x = (r - r_{\text{gap}})/\text{gap width}$, and we assume the gap width to be $2 \times H$, where H is the gas scale height, given as $H = c_s/\Omega$. Additionally, we test various “depths” of the gap by varying the α gap as some factor $\times \alpha_0$ ($=1 \times 10^{-3}$). We choose three gap depths in our simulations: $1.5 \times \alpha_0$, $10.0 \times \alpha_0$, and $75.0 \times \alpha_0$. We find these depths to be equivalent to a range in depletion in Σ_g in the gap of (i) a \sim few times, (ii) one order, and (iii) two orders of magnitude, respectively. We anticipate that these ranges in gas depletion are also likely to be distinct enough that they may be

Table 1
Table of Parameters Used in Our Simulations

Model Parameter	Symbol	Parameter Value/Range
Disk Parameters		
Inner disk radius	R_{in}	0.1 au
Characteristic radius	R_0	70 au
Outer disk radius	R_{out}	500 au
Initial disk mass	M_{disk}	$0.05 M_{\odot}$
Initial gas surface density at $R_0 = 70$ au	Σ_0	14.3 g cm^{-3}
Initial gas surface density power-law index		-1
Disk viscosity	α	$5 \times 10^{-4}, 10^{-3}, 5 \times 10^{-3}$
Opacity (fine dust)	κ	$5 \text{ cm}^2 \text{ g}^{-1}$
Simulation time		5 Myr
Dust Parameters		
Initial monomer size	a_p	0.1 μm
Internal particle density (ices, silicates)	ρ_s	1.5 g cm^{-3}
Initial solid particle surface density	$\Sigma_{\text{icy dust}}, \Sigma_{\text{dust}}$	$0.005 \times \Sigma_{\text{gas}} \text{ g cm}^{-2}$
Fragmentation velocity	v_f	1, 5, 10 m s^{-1}
Schmidt number for diffusion	Sc_p	0.3, 1.0, 3.0
Vapor Parameters		
Initial concentration of water vapor	c	1×10^{-4}
Schmidt number for diffusion	Sc_v	0.3, 1.0, 3.0
Gap Parameters		
Gap location	R_{gap}	7, 15, 30, 60, 100 au
Gap depth	α_{gap}	$1.5 \times \alpha_0$ (shallower), $10 \times \alpha_0, 75 \times \alpha_0$ (deeper); $\alpha_0 = 1 \times 10^{-3}$
Gap width		$2 \times \text{scale height}$
Time when gap instantaneously forms	t_{gap}	0 Myr

Note. Bold values indicate fiducial model parameters.

observationally distinguishable (e.g., see CO depletions in high-resolution MAPS images in Figures 18 and 20 in Zhang et al. 2021; and Figure 4 in Wölfer et al. 2023). These gap depths in turn likely correspond to the presence of planet of mass $33 M_{\oplus}$, $0.3 M_J$, and $\geq 1.0 M_J$, respectively, within the gap, when compared to the numerical simulations done by Zhang et al. (2018; see their Figure 2).

Note that we use the Gaussian α peak only for creating and maintaining the gap in the gaseous disk, and otherwise assume that α is uniform for all other physical processes, including setting the thermal structure (Equation (5)), dust diffusion (Equation (11)), as well as calculating the maximum particle size in the fragmentation regime (Equation (9)).

We assume that streaming instability is the dominant mechanism of particle clumping leading to planetesimal formation (Bai & Stone 2010). We also note that massive planets embedded in disks larger than $\sim 5 M_J$ can interact with the gas, and may even lead to the formation of an eccentric disk, likely depending on the disk viscosity ν (Kley & Dirksen 2006; Ataiee et al. 2013; Teyssandier & Ogilvie 2017; Bae et al. 2019). Particles in such eccentric rings may undergo more fragmentation (Zsom et al. 2011) and may not efficiently be trapped beyond the gap. We therefore make the assumption that the gap-forming planets in our simulations are much smaller than $5 M_J$.

2.2. Dust Evolution and Transport

To incorporate dust growth and fragmentation, we adapt the two-population model of Birnstiel et al. (2012), which reproduces the results of detailed full numerical simulations (Birnstiel et al. 2010) that include growth, fragmentation, and the radial drift of dust grains (with the advantage of being not as computationally expensive). Dust grains start from monomer sizes of $0.1 \mu\text{m}$ at the start of the simulation and which grow with time, with their rate of growth dependent on the local dust density. They grow to a maximum size that is typically limited by either fragmentation in the interior of the disk or by radial drift in the outer regions. The fragmentation limit is set by the fragmentation threshold velocity v_f that we assume to be independent of particle size, based on laboratory experiments (Güttler et al. 2010). We assume that v_f is uniform throughout the disk, or varying at the snow line where particles lose their icy content, which allows us to account for a range of stickiness of icy silicates. We discuss this in more detail in the next subsection.

The general treatment of radial transport of dust particles (including advection-diffusion and radial drift) is similar to that implemented in Kalyaan et al. (2021) and Birnstiel et al. (2012). We assume that the diffusivities of the dust particles are similar to the gas diffusivity, fulfilled at the limit of $St < 1$ (Birnstiel et al. 2012, see their Appendix A). We also note that we use the same radially uniform α (1×10^{-3}) for dust diffusion, as well as for calculating the maximum grain size in the fragmentation limit.

2.3. Icy Particles

As done in Kalyaan et al. (2021), we implement two particle populations—one entirely made of water ice, and the other made entirely of silicates, in order to simulate icy silicate particles that have an icy mantle around a silicate core. The ices in these particles sublime when they drift inwards and eventually approach warmer temperatures surrounding the water snow line region in the disk (a few au from the star). In the previous model, we assumed that these two particle populations would be equally abundant and be identical in particle size, and therefore move similarly. In the current model, we replicate the same effect by tracking the fraction of water ice in the total incoming particle mass at the snow line. We calculate $f_{\text{H}_2\text{O}}$ as follows:

$$f_{\text{H}_2\text{O}}(r) = \frac{\Sigma_{\text{icy}}}{\Sigma_{\text{icy}} + \Sigma_{\text{dust}}}. \quad (8)$$

Then, we assume a fragmentation velocity threshold v_f based on our assumptions of the relative strength of icy silicate particles compared with bare silicate particles. We allow for two possibilities: either that icy particles are stickier and have a higher v_f (up to an order of magnitude, i.e., 10 m s^{-1}) compared to silicates (1 m s^{-1}) or that they are both roughly comparable to each other. In the former case, we calculate $f_{\text{H}_2\text{O}}(r)$ to track the bulk water abundance in particles. If $f_{\text{H}_2\text{O}}(r) < 0.1$, then $v_f(r)$ is assumed to be 1 m s^{-1} . If $f_{\text{H}_2\text{O}}(r) > 0.1$, then $v_f(r)$ is assumed to be 10 m s^{-1} . In the latter case, we consider that v_f is uniform irrespective of distance from the star and consider a range of radially constant v_f ranging from 1–10 m s^{-1} . Overall, we still maintain a water ice abundance (by mass) in the incoming particle distribution that is roughly 50% in ice and silicates in the outer disk beyond the snow line. (We note that

our results do not change for any chosen $f_{\text{H}_2\text{O}}$ threshold values < 0.4 , due to the steep decrease in $f_{\text{H}_2\text{O}}$ at the snow line in our models.)

For both ice and silicates, we assume that $\rho_s = 1.5 \text{ g cm}^{-3}$.

2.4. Planetesimal Formation

We incorporate planetesimal formation as follows. We adopt the same prescription as in Drazkowska et al. (2016; their Equation (16)) for computing the mass of planetesimals that forms from dust at each radial location, but in place of their stricter conditions dictating where and when planetesimals can form, we adopt the latest criteria from streaming instability simulations by Li & Youdin (2021). In this work, the authors find that the value of Z (i.e., Σ_d/Σ_g) where strong clumping can take place depends on the Stokes number St , and find that clumping can take place at lower Z values for a specific range of St than previously thought. We use their prescribed fit from their Equation (11) (depicted in their Figure 4(b)) along with Equation (14). We use these criteria for planetesimal formation even in the pressure bump (which they are not intended for due to a lack of similar criteria for pressure bumps (e.g., Carrera & Simon 2022), and admit that we may overestimate planetesimal formation at the pressure bump region. (In Section 3.7, we discuss in detail how planetesimal formation at the pressure bump region does not matter much for our results, as our traps block the passage of particles efficiently.)

We note that once planetesimals form, they are immobile and remain in place where they form, i.e., we do not consider any subsequent migration or dynamical evolution of planetesimals. They also do not accrete any pebbles.

3. Results

In this work, we perform a detailed parameter study to investigate the effect of relevant disk/gap or vapor/particle parameters, such as gap location, gap depth, fragmentation velocity, viscosity α , and particle and vapor diffusivity on the time-evolving vapor enrichment in the inner disk. We also explore the effect of including planetesimal formation, and the presence of multiple gaps. In each subsection, we go through the effect of systematically varying each of the abovementioned parameters while keeping the others constant (see Table 1), and discuss the most significant insights in Section 4. (In all our simulations, we assume that the depth of the gap is given by $10 \times \alpha_0$, where fiducial $\alpha_0 = 1 \times 10^{-3}$ unless stated otherwise. We also assume that the fiducial fragmentation velocity threshold v_f in simulations with dust growth and fragmentation is 5 m s^{-1} .)

3.1. Without Dust Growth and Fragmentation

We begin our study by exploring the effect of including the growth and fragmentation of dust particles in uniform disks (without gaps), and show simulations without these physical processes in Figure 2 and with them in Figure 3 (see black dashed lines).

These results are plotted as ‘‘vapor enrichment’’ (i.e., the mass of vapor present in the inner disk within the snow line region at any time, normalized to the mass of vapor present within the snow line at time $t = 0$) in the left panel, and ‘‘vapor abundance’’ (i.e., the mass of vapor with respect to the mass of bulk gas within the snow line at each time) in the right panel (see also Appendix A). Note that in our model, water vapor can

only be present in the inner disk within the snow line. Moreover, since the temperature in the disk varies with time, the snow line also moves slightly inward with time (see Appendix C and Figure 13 in Kalyaan et al. 2021).

In the simulations shown in Figure 2, the entire dust population is composed of 1 mm particles. As discussed previously in Kalyaan et al. (2021), we find that the mass of vapor and its abundance in the inner disk evolves with time as icy pebbles drift inward and deliver water vapor into the inner disk. Inner disk vapor mass and its abundance climbs and reaches a peak as the bulk of the pebble mass enters the inner disk, and subsequently declines with time as stellar accretion takes over and depletes the inner disk of vapor.

In a uniform disk without gaps, the bulk of the same-sized dust population would drift inward around the same time (here ~ 2 Myr) depending on their radial location in the disk. On the contrary, including the processes of growth and fragmentation (see Figure 3) results in particles of a range of sizes. Larger pebbles drift more rapidly than smaller particles, leading to an earlier start in vapor enrichment, as well as a more intense but shorter enrichment episode. The intensity of enrichment may depend on how large the particles become before they fragment (see Section 3.4).

In the following subsection, we will compare the effect of dust growth and fragmentation on vapor enrichment in disks with gaps.

3.2. Varying Radial Location of Gaps

We next vary the radial location of the gap in our simulations with and without the growth and fragmentation of dust particles. As in the previous work (Kalyaan et al. 2021), we choose several gap locations from the inner to the outer disk, i.e., 7, 15, 30, 60, and 100 au from the star, to explore the fullest possible extent of the effect of structure on the mass of vapor in the inner disk. As we will explain below, we find that in spite of the initial disk size being 500 au, gaps farther than the critical radius have very little effect on the inner disk vapor mass (in our case the gap at 100 au).

The results in both Figures 2 and 3 follow the increase in mass of vapor brought to the inner disk, then the peak of vapor enrichment when the bulk of the drifting mass reaches the inner regions, followed by depletion with time. This profile is especially prominent in the case of a disk with no gap, where the peak vapor enrichment is highest from the initial value. With a gap, however, both the peak value of the vapor enrichment and the time it is attained may be different depending on where the gap is located. A closer-in gap (of equal depth) severely restricts the entry of ice-bearing pebble mass into the inner disk, as seen by the peak vapor enrichment for the disk with a 7 au gap at only ~ 1.6 at time ~ 0.07 Myr in the simulations with growth and fragmentation. At the same time, gaps farther out do not filter out as much pebble mass into the inner disk. This is because as they are further out, they do not block as much material as the gaps that are present closer in. Moreover, pressure bumps farther out have a shallower pressure gradient, as the width of the gaps depends on the scale height at that radial location, which increases with r . Therefore, the further they are, the water enrichment profiles for these outer gaps more and more begin to resemble the no-gap scenario, both in value and time of peak vapor enrichment.

For a single-sized dust population, the radial location of the gap (for gaps of similar depths) determines the smallest particle

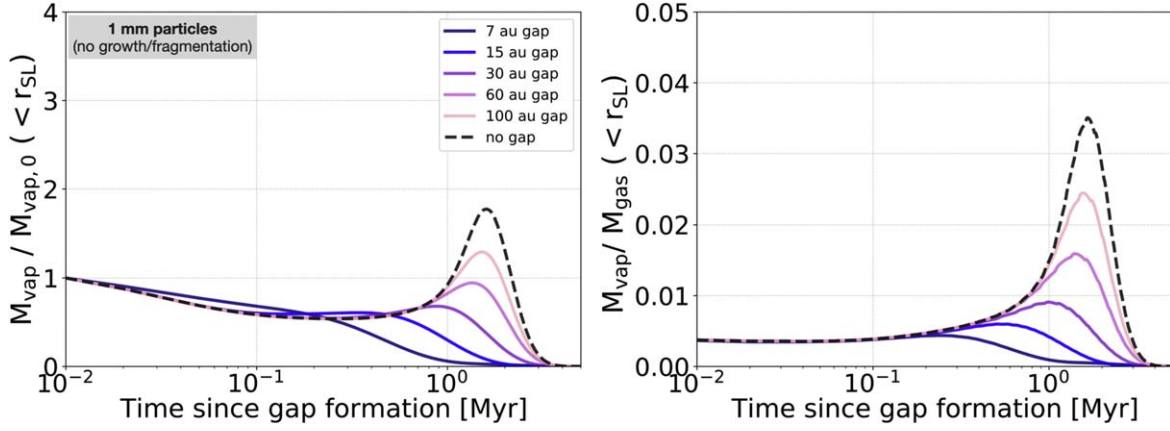


Figure 2. The left panel shows the time evolution of vapor enrichment in the inner disk, i.e., the mass of water vapor within the snow line region at time t , normalized to the mass of water vapor within the snow line at time $t = 0$, for simulations without dust growth or fragmentation. The right panel shows time evolution of vapor abundance, i.e., mass of vapor within the snow line region normalized to the mass of gas within the snow line region, for the same simulations. Different colors denote profiles for simulations where the gap is located at different radii. The black dashed line shows the case with no gap for comparison.

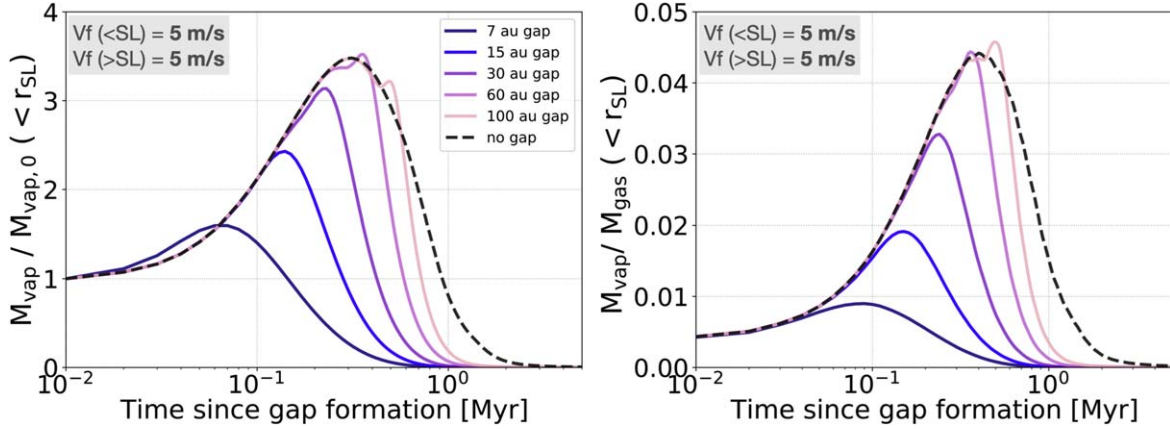


Figure 3. The left panel shows the time evolution of vapor enrichment in the inner disk, i.e., the mass of water vapor within the snow line region at time t , normalized to the mass of water vapor (within the snow line) at time $t = 0$, for simulations with dust growth and fragmentation. The right panel shows the time evolution of vapor abundance, i.e., the mass of vapor within the snow line region normalized to the mass of gas within the snow line region for the same simulations. Different colors denote profiles for simulations where the gap is located at different radii. The black dashed line shows the case with no gap for comparison. Fiducial $v_f = 5 \text{ m s}^{-1}$ both inside and outside of the snow line is assumed.

size it is able to trap and block from passing through (see Figure 12 in Kalyaan et al. 2021). With increasing radial distance r , the ability of a similar gap to block smaller particles gets progressively better. This is because smaller particles have larger St with increasing r , and are therefore easier to trap in pressure bumps. Additionally, they also diffuse less at greater distances (due to higher St). Therefore, for the same-sized particles, inner gaps are leakier than outer gaps. This is consistent with earlier theoretical predictions from Pinilla et al. (2012) who found a critical size of particles trapped in the pressure bump that decreased with increasing r , and is also consistent with observations that find a correlation between spectral index α_{mm} and cavity radius (Pinilla et al. 2014).

When the physics of particle growth and fragmentation is included, even if the gap is present in the drift-dominated regime (applicable for our outer gaps between 15 and 100 au for fiducial v_f), the fragmentation limit is always (eventually) reached in the pressure bump, replenishing the population of small particles within the bump. As outer gaps are better at trapping smaller particles, more of the small particles pass through the inner gap than through the outer gaps. The inner

gaps are therefore slightly leaky compared to the outer gaps. (See also Appendix C and Figure 14.)

Overall, for the same gap depth, vapor enrichment in the inner disk is affected by where the gap is located in the outer disk. If it is present too far out, it may not block enough icy particles to have any effect. An inner gap (in spite of being slightly leaky) may still block the most amount of icy particles outside of the gap.

We also note the presence of very small surges in water vapor enrichment that slightly overshoot the no-gap profile, most noticeable for gaps in the outer disk (>60 au). These small surges arise from keeping the initial disk mass the same across all simulations whether or not gaps are present. Therefore, in the case of the disk with a gap further out, the disk mass inside of the gap is higher in comparison to the no-gap case.¹³ In this work, we keep the magnitude of these surges negligible by keeping the depth of the gaps in most of the simulations in this work limited to $10 \times \alpha_0$. As we will explain later in Section 3.3, choosing a higher gap depth has little to no

¹³ We also find these small surges to be present in at least one other study (Andama et al. 2022).

impact on the resulting time-evolving vapor enrichment in the inner disk. From here, we only show the vapor enrichment plots throughout the rest of the paper. This is because the snow line region moves inward with time, making the mass of gas within the snow line a constantly varying quantity. We therefore use “vapor enrichment,” i.e., the mass of vapor normalized to its value at the initial time, rather than vapor-gas abundance, for the purpose of comparing across simulations (see Appendix A).

3.3. Varying Gap Depth

For specific radial gap locations, we also vary the depth of the gap by parameterizing the turbulent viscosity α at the center of the gap as a factor $\times \alpha_0$. As mentioned before, we select three gap depths: $1.5 \times \alpha_0$, $10 \times \alpha_0$, and $75 \times \alpha_0$ for gaps located at 7, 30, and 100 au, respectively, as seen in Figure 4. We find that varying the gap depth matters most for the innermost gaps, as seen in the case of 7 au (left panel). At this gap location, a shallow gap ($1.5 \times \alpha_0$) makes for a highly inefficient barrier that allows for the passage of material for several million years after gap formation. For any values of the gap depth $\geq 10 \times \alpha_0$, the gap becomes very efficient at blocking the passage of dust material and the water enrichment profiles become identical. Other gap locations (e.g., 30 au or 100 au shown in the middle and right panels, respectively) already show little deviation from the no-gap water enrichment profiles simply due to the smaller amount of ice-rich material they block based on their location. Over and above this, a shallower gap yields a very small deviation in the vapor enrichment profile relative to that seen with deeper gaps in the outer disk. In the case of shallow gaps, small particles pass through them (see Appendix B). This leakage of material results in the high vapor enrichment peaks for simulations with shallow gaps.

Overall, varying the gap depth has the strongest effect on the innermost gaps. A deep inner gap can block a lot of ice-rich dust material from entering the inner disk, while a very shallow gap can let small particles pass through, yielding enrichment profiles that resemble that of a disk without any gaps.

3.4. Varying Fragmentation Velocity

As mentioned before, we take into account a range of assumptions for the relative fragmentation velocity thresholds v_f for ices and silicates in this work. We consider two different cases: (i) that icy particles are stickier than silicate particles, and therefore have $v_f = 10 \text{ m s}^{-1}$ (an order of magnitude higher than silicate particles, which have $v_f = 1 \text{ m s}^{-1}$); and (ii) that icy and silicate particles both have comparable tensile strengths against collisions, and therefore have similar v_f . In this latter case, as explained before, v_f is assumed identical for ices and silicates, i.e., constant both inside and outside of the snow line. Here, we test a range of constant v_f values: 1, 5, and 10 m s^{-1} . We show these results in the third row of Figure 5, for the fiducial value of turbulent viscosity $\alpha = 1 \times 10^{-3}$, where the first three columns correspond to $v_f = 1, 5, \text{ and } 10 \text{ m s}^{-1}$ for both ices and silicates, respectively, and the last column corresponds to the case where $v_f = 10 \text{ m s}^{-1}$ for ices and $v_f = 1 \text{ m s}^{-1}$ for silicates. As before, for each case, we perform simulations with gaps at the same radial locations.

We find that for a constant $v_f(r) = 1 \text{ m s}^{-1}$, the water vapor enrichment profiles show negligible deviation between simulations with or without a gap, irrespective of gap location, and

simply decrease with time over 5 Myr from their initial value at $t = 0$. For a constant $v_f(r) \geq 5 \text{ m s}^{-1}$, the vapor enrichment profiles show the familiar increase, peak, and decrease as drifting pebbles deliver ice-rich material into the inner disk, and the ice sublimates to vapor at the snow line. With a gap, as we found before, the vapor enrichment from the initial time can be significantly lower or slightly lower relative to the no-gap scenario, depending on gap location.

The vapor enrichment profiles from simulations with radially constant v_f values of 5 and 10 m s^{-1} vary in the following two ways. Higher v_f can result in a slightly higher no-gap peak, i.e., $4 \times$ the the initial value for 10 m s^{-1} , compared to $3.5 \times$ initial value for 5 m s^{-1} . Higher v_f results in earlier peak times: ranging from ~ 0.1 Myr after gap formation for the no-gap case to 0.02 Myr for a 7 au gap for 10 m s^{-1} , compared to 0.3 Myr for no gap to 0.06 Myr for a 7 au gap for 5 m s^{-1} , with the peaks for the cases with other gap locations falling in between these two times for each v_f . These variations in vapor enrichment for different v_f values occur because the maximum particle size at the fragmentation limit a_{frag} is given as follows (Birnstiel et al. 2012, Equation (8)):

$$a_{\text{frag}} \propto \frac{2}{3\pi} \frac{\Sigma v_f^2}{\rho_s \alpha c_s^2}, \quad (9)$$

where Σ is the gas surface density, ρ_s is the internal particle density, and c_s is the sound speed. Alternatively, the Stokes number at the fragmentation limit St_f is given by

$$St_f = \frac{1}{3} \frac{v_f^2}{\alpha c_s^2}. \quad (10)$$

Here, a_{frag} and St_f are proportional to v_f^2 . As v_f is increased, small particles are able to grow to larger and larger sizes before they fragment. These larger particles are able to drift inward more rapidly and also bring in more water with them more quickly as they drift, therefore showing higher and earlier peak vapor enrichment with increasing v_f . (In all our simulations, the inner few au are always in the fragmentation-dominated regime.)

The case with 1 m s^{-1} is exceptional as such a low v_f allows for very little growth of particles. Most of the disk is at the fragmentation-dominated limit. These particles drift very slowly (slower than gas accretion onto the star) that the inner disk is never really enriched with water vapor over the value at $t = 0$, causing the vapor enrichment to decline continuously with time (see also Appendix A). Finally, we explore different v_f for ices and silicates, and find these results to be identical to that of constant $v_f = 10 \text{ m s}^{-1}$. This is because the mass of water that is brought inwards in both of these cases is the same as what matters most in our simulations is the fragmentation velocity of icy particles.

Overall, for moderate values of the turbulent viscosity α , lower $v_f (= 1 \text{ m s}^{-1})$ yields similar vapor enrichment profiles, whether or not gaps are present. Higher v_f show distinct differences in these profiles that are dependent on the presence of a gap and their radial location.

3.5. Varying Viscosity

Figure 5 shows not only the full simulation grid with various gap locations we performed for a range of v_f values but it also includes simulations performed for a range of turbulent

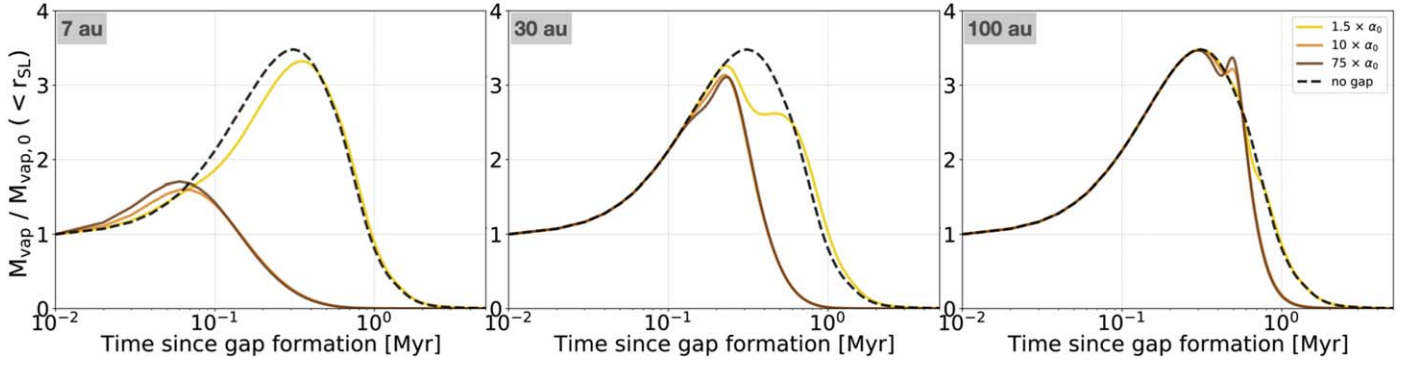


Figure 4. Time evolution of vapor enrichment for different gap depths at three different radial locations: 7 au (left panel), 30 au (middle panel), and 100 au (right panel). Different colors denote different gap depths (yellow denotes a shallower gap and brown denotes a deeper gap than fiducial). The black dashed line shows the case with no gap for comparison. Fiducial $v_f = 5 \text{ m s}^{-1}$ both inside and outside of the snow line is assumed.

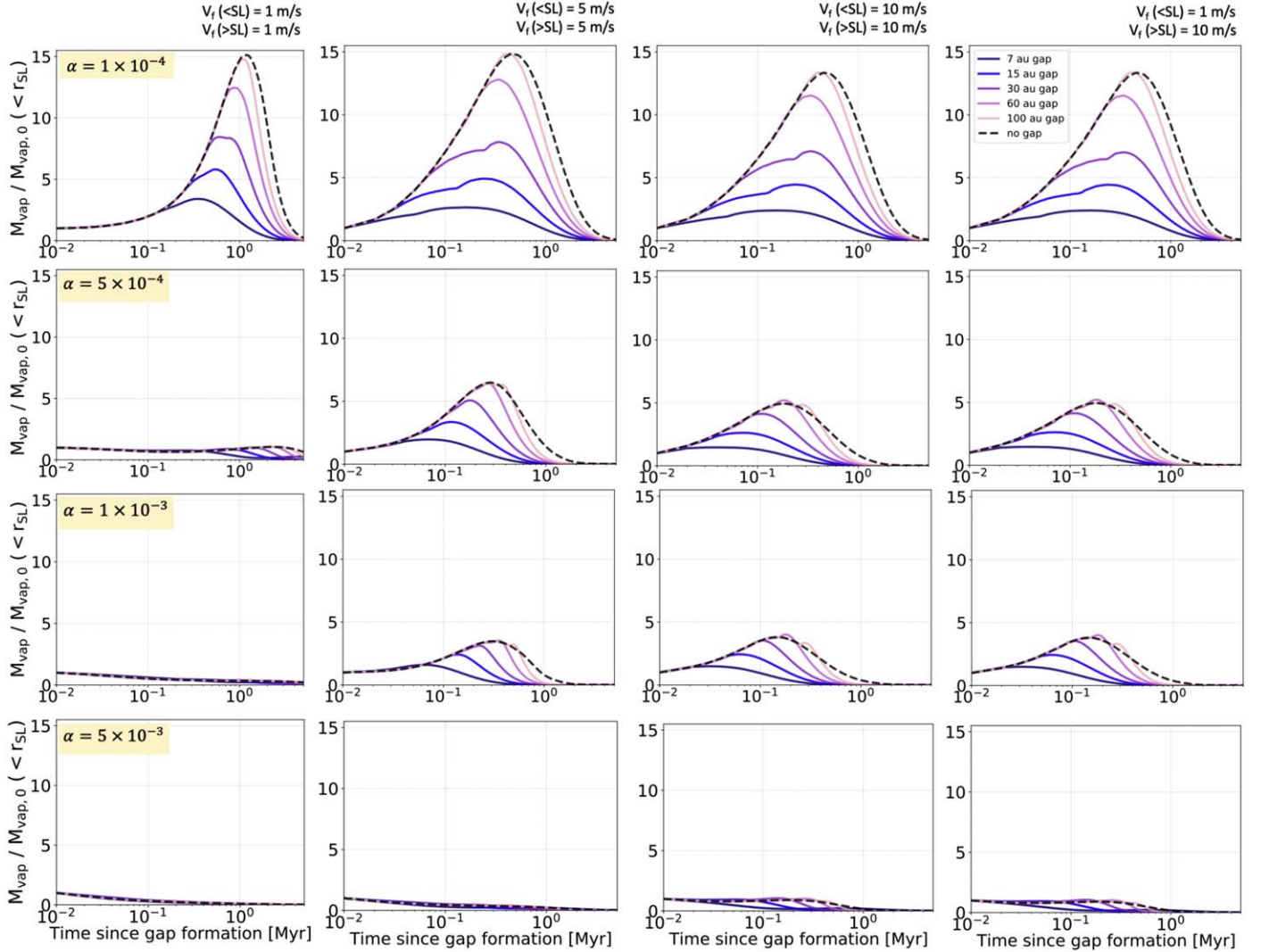


Figure 5. Grid of simulations performed for a range of fragmentation velocity v_f , and turbulent viscosity α . Rows from top to bottom show simulations for $\alpha = 1 \times 10^{-4}$, 5×10^{-4} , 1×10^{-3} , and 5×10^{-3} , respectively. The first three columns from left to right show $v_f = 1 \text{ m s}^{-1}$, 5 m s^{-1} , and 10 m s^{-1} (for both inside and outside the snow line). The last column shows the case with $v_f = 1 \text{ m s}^{-1}$ inside the snow line and 10 m s^{-1} outside of it. Colors and lines are as in Figure 3. Note that Figure 3(a) is reproduced in the second panel of the third row to show the complete grid.

viscosity α . Overall, we explored four values of α ranging over an order of magnitude (1×10^{-4} , 5×10^{-4} , 1×10^{-3} , and 5×10^{-3}), suggested from observations (see Table 3 in Rosotti 2023), to study how low or high α may impact vapor

enrichment in the inner disk. Results for these additional values of α are shown in the first, second, and fourth rows of this grid.

For lower α (than fiducial), we find that the vapor enrichment peaks are higher than with fiducial α , reaching up

to 5–6.5 for an α of 5×10^{-4} , and reaching up to 14–15 for an α of 1×10^{-4} for the no-gap profiles with $v_f = 5$ and 10 m s^{-1} . Even the 1 m s^{-1} simulations show an increase in vapor enrichment over the initial time. While the enrichment episode is only slight for $\alpha = 5 \times 10^{-4}$, it is substantially higher peaked for lower $\alpha = 1 \times 10^{-4}$, before decreasing eventually.

In contrast, for higher α ($=5 \times 10^{-3}$), vapor enrichment declines from the initial time for all v_f values. Only the cases with $v_f = 10 \text{ m s}^{-1}$ show that vapor enrichment in the disk stays at ~ 1 for 0.2–0.3 Myr after gap formation, and then decreases with time between 0.1 and 1 Myr depending on if there is a gap and where it is located.

These effects can again be attributed to how α is inversely proportional to a_{frag} and St_{frag} in Equation (9). Higher α therefore results in a lower fragmentation size limit, and slower drift for particles in the disk, and vice versa.

3.6. Varying Particle/Vapor Diffusivity

We also perform some simulations where we study the effect of varying the diffusivities of the particles and vapor, while keeping the fiducial value of α . For particles, the diffusivity $\mathcal{D}_{\text{part}}$ is generally taken to be $\mathcal{D}_{\text{part}} = \mathcal{D}_{\text{gas}}/(1 + \text{St}^2)$. In our simulations, St is always $\ll 1$, and reaches a maximum of 0.1 in the outer disk at few tens of au. We therefore take $\mathcal{D}_{\text{part}} \approx \mathcal{D}_t$, which is given as

$$\mathcal{D}_t = \frac{\nu}{\text{Sc}_t}. \quad (11)$$

Here, ν is the viscosity of the bulk disk gas and Sc denotes the Schmidt number of the tracer t in the bulk gas, which refers to either particles or vapor in the disk. We vary Sc for particles as well as for vapor (i.e., Sc_p and Sc_v , respectively) over an order of magnitude around the fiducial value of 1 and show the results of our simulations in Figure 6, where the top row shows simulations varying Sc_p and the bottom row shows simulations varying Sc_v . Here, varying Sc_p (or equivalently $\mathcal{D}_{\text{part}}$) physically implies that particles are more or less diffusive in the gaseous medium as they drift inward in the inner disk. Upon reaching the inner disk within the snow line, the ice in these particles sublimates to form vapor that yields these vapor enrichment profiles. Varying Sc_v , on the other hand, takes into account how diffusive vapor is in the bulk gas after it is generated at the snow line and moves through the inner disk within the snow line region. As lower Sc implies higher diffusivity, the panels on the left (both Sc_p and Sc_v simulations) show that the vapor enrichment profiles are more shallow and spread out in time, compared to the profiles in the panels on the right, which show generally higher peak enrichment for the no-gap and gap simulations. However, varying Sc_v seems to have a more significant impact (with peak enrichment reaching ~ 4.0 for $\text{Sc}_v = 3.0$ and over ~ 3.0 for $\text{Sc}_v = 0.3$) than varying Sc_p , which shows comparatively little change (with peak enrichment reaching ~ 3.5 for $\text{Sc}_p = 3.0$ compared to ~ 3.3 for $\text{Sc}_p = 0.3$) in spite of a change of an order of magnitude in Sc_p .

Overall, the effect of changing the vapor or particle diffusivity is relatively small; the particle size set by α through fragmentation is more important in determining whether dust is trapped.

3.7. Including Planetesimal Formation

To study the effect of including the physics of planetesimal formation in our simulations on the vapor enrichment in the inner disk, we perform a series of simulations with a range of v_f , where we assume that v_f both inside and outside of the snow line is 5, 10, or 15 m s^{-1} (shown in the top, middle, and bottom rows of Figure 7, respectively). The choice of v_f here plays an important role as it sets how big particles can grow before they fragment. The size of the particles (or equivalently the Stokes number of the particles) is critical for fulfilling the criteria for strong clumping as explored in Li & Youdin (2021). As v_f is increased, more planetesimal formation takes place in regions where adequate dust-to-gas ratios of sufficiently large particles are reached. In our simulations, these conditions are satisfied in either one or two of the following regions: (i) in the pressure bump beyond the gap where particles drifting inward from the outer disk are continuously being accumulated, grown, and trapped; and (ii) just beyond the snow line where there is an overdensity of ice mass in particles due to retro-diffusion of vapor out through the snow line (Ros & Johansen 2013; Schoonenberg & Ormel 2017). We show vapor enrichment profiles on the first column of Figure 7, corresponding to the total mass of planetesimals formed (in the entire disk) over time for each simulation in the second column, the total planetesimal mass formed at 5 Myr at either the snow line region or pressure bump beyond the gap in the third column, and finally the fraction of water ice in planetesimals formed at either location in the fourth column. We also additionally show when planetesimal formation takes place beyond the snow line or at the bump in Appendix D and Figure 15.

For $v_f = 5 \text{ m s}^{-1}$, we find that the vapor enrichment profiles (top-left subplot) are identical to the corresponding simulations without planetesimal formation shown earlier in Figure 3. In these simulations, the conditions for strong clumping and planetesimal formation are only reached at the pressure bump beyond the gap. These particles are otherwise trapped beyond the gap anyway throughout the simulation. Therefore, there is no effect on pebble delivery as well as on vapor enrichment in the inner disk. For these simulations, no planetesimals form in the disk for the no-gap simulation. But for disks with a gap, the final planetesimal mass formed beyond each gap decreases with increasing radial distance of the gap. This is because more dust mass can accumulate and grow beyond the gap if the gaps are closer in. The total final planetesimal mass beyond a disk with a 7 au gap is $\sim 150 M_{\oplus}$, decreasing to $\sim 40 M_{\oplus}$ for a disk with a gap at 100 au. Furthermore, planetesimals form in the trap between 0.1 and 1 Myr for all these simulations.

For simulations with $v_f = 10 \text{ m s}^{-1}$, a small mass of planetesimals ($< 10 M_{\oplus}$) form after 0.07 Myr just beyond the snow line even for the case with no gap. Among the gap simulations, we find that for simulations with an inner gap at 7 or 15 au, planetesimals form only beyond the pressure bump. For simulations with an outer gap (30, 60, or 100 au), we find that planetesimals form beyond the pressure bump as well as just beyond the snow line region. In these three cases, the peak enrichment (~ 3.2 – 3.5) are smaller than those of corresponding simulations without planetesimal formation (~ 3.5 – 4.0), as some icy material is sequestered in planetesimals just beyond the snow line that would have otherwise been delivered into the inner disk and enriched it with water vapor. It is also important to note that a farther out gap allows for some planetesimal formation at the snow line (up to $\sim 10 M_{\oplus}$ for the 100 au gap),

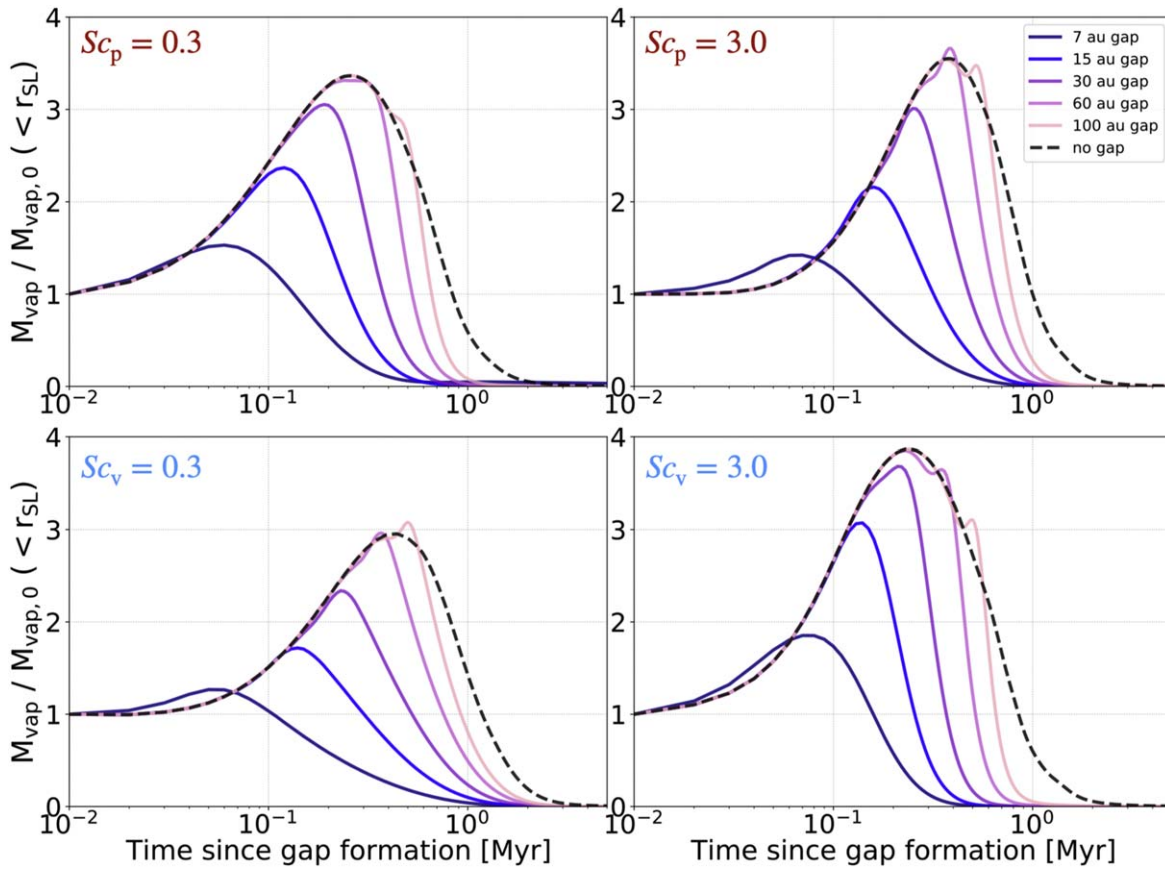


Figure 6. Time evolution of vapor enrichment for simulations performed with a range of particle and vapor diffusivities. The top row shows simulations varying the particle diffusivity; the bottom row shows simulations varying the vapor diffusivity. Fiducial $v_f = 5 \text{ m s}^{-1}$ both inside and outside of the snow line is assumed. Colors and lines are as in Figure 3.

rather than a close-in one. In these simulations, planetesimals begin to form at different times for disks with gaps at different locations (see Appendix D, Figure 15). Planetesimal formation at the pressure bump can begin as soon as the gap is formed (i.e., $t = 0$) for a closer-in gap (7 au), and as late as 0.4 Myr for an outer gap (100 au). Planetesimal formation at the snow line only proceeds for a very short duration ($\sim 10,000$ yr) at around 0.1 Myr. For the dust trap, on the other hand, it can begin at the start of the simulation ($t = 0$), for the disk with a closer-in 7 au gap and proceed until 1 Myr after gap formation, or start at around 0.35 Myr and proceed until 1 Myr after gap formation, for a disk with an outer gap at 100 au.

Finally, we additionally explore an even higher value of $v_f = 15 \text{ m s}^{-1}$ and find that for all simulations with and without a gap, mass of planetesimals formed at the dust trap is similar to the previous case ($v_f = 10 \text{ m s}^{-1}$). However, additionally, a significant mass of planetesimals forms just beyond the snow line, as well as just beyond the gap, if a gap is present. The amount of mass locked up in planetesimals just beyond the snow line is sufficient to cause a drastic decrease in the vapor enrichment profiles in the inner disk for all runs with different gap locations, such that they do not peak beyond ~ 1.6 for even the no-gap and outer gap simulations.

Generally, we find that similar masses of planetesimals are formed in dust traps for a range of v_f , and that higher v_f allows more planetesimal formation at the snow line. We also find that planetesimals formed at the pressure bump beyond the gap have a 50%–50% ice-to-rock ratio, in comparison to ice-rich planetesimals that form just beyond the snow line with 90%

water ice via retro-diffusion or the cold-finger effect. This is consistent with results obtained from previous studies (Stevenson & Lunine 1988; Cuzzi & Zahnle 2004; Ros & Johansen 2013) as well as recent work exploring the origin of CO-ice-rich comets beyond the CO snow line (Mousis et al. 2021). Other studies have also investigated planetesimal formation at the snow line. In a smaller disk, Schoonenberg et al. (2018) found that icy planetesimals that formed beyond the snow line dominated the total mass ($\sim 100 M_\oplus$) when compared with rocky planetesimals ($\sim 1 M_\oplus$) that formed within the snow line region. They also found that the planetesimal formation proceeded for around 1000–10,000 yr. Lichtenberg et al. (2021) found two distinct reservoirs of planetesimals that could form by the outward and subsequent inward migration of the snow line across the disk. They argued that one reservoir forms mainly by the cold-finger effect at 1.3–7.5 au from 0.2–0.35 Myr and is composed of $\sim 1 M_\oplus$, and a second reservoir of planetesimals of $\sim 300 M_\oplus$ forms by inward drift and the pile-up of pebbles between 3 and 17 au from 0.7 Myr onwards. Our results show some similarities and some key differences from these studies. We find that two reservoirs are possible if we consider a higher v_f ($\geq 10 \text{ m s}^{-1}$), where a smaller ice-rich mass of planetesimals originating from retro-diffusion (or the cold-finger effect) can form at the snow line, and a much larger reservoir of $\sim 100 M_\oplus$ can form within the dust trap beyond a gap. The mass of planetesimals beyond the gap is dependent on the radial location of the gap, i.e., if the gap is closer in, planetesimal formation can start earlier and

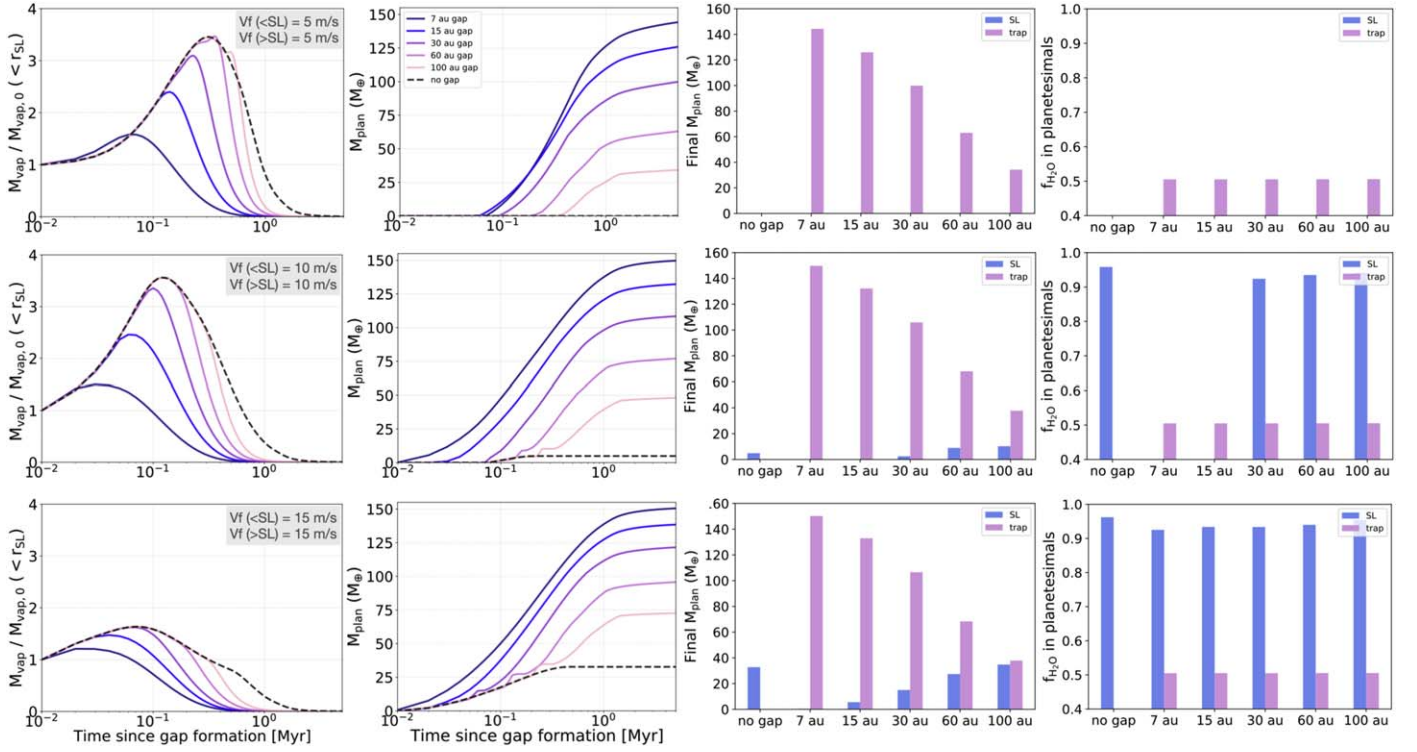


Figure 7. Plots with the results of simulations with planetesimal formation for fiducial initial disk mass $M_{\text{disk}} = 0.05 M_{\odot}$. The first column shows the time evolution of vapor enrichment for the same simulations performed with planetesimal formation. The second column shows the corresponding total mass of planetesimals formed over time. The third column shows the final planetesimal mass formed at the trap beyond the gap or the snow line (SL) region, for each simulation with the gap at different radial locations. The fourth column shows the final fraction of water ice in the planetesimals that formed at the snow line or the dust trap. The top, middle, and bottom rows, respectively, correspond to $v_f = 5, 10,$ and 15 m s^{-1} , inside and outside of the snow line. Line colors are as in Figure 3.

proceed for longer, resulting in more planetesimal mass being formed.

Recent studies (Carrera et al. 2021; Carrera & Simon 2022) argue that particles smaller than centimeter sized may not lead to planetesimal formation in rings. It is therefore likely we are overestimating planetesimal formation at the dust trap, especially beyond the outermost gaps (i.e., 100 au) where particles are largely millimeter sized or smaller. However, as mentioned before, planetesimal formation at the dust trap has little effect on vapor enrichment in the inner disk.

Overall, our simulations suggest that planetesimal formation is only significant if it occurs at the snow line region, and it does not matter for vapor enrichment in the inner disk if it occurs in the dust trap beyond the gap.

3.8. Exploring Multiple Gaps

We finally also explore how the presence of additional gaps in the outer disk can affect the water enrichment in the inner disk (with planetesimal formation). From data in the observational surveys of protoplanetary disks with gaps from Huang et al. (2018) and Long et al. (2018), we find that gap locations span a wide radial range and peak around 40 au. We therefore select 10, 40, and 70 au as three representative radial locations to introduce one, two, or three gaps in our disk simulations, as, respectively, presented in the left, middle, and right panels of Figure 8.

We first consider the effect of multiple gaps where all the gaps are of the same gap depth, i.e., a fiducial value of $10 \times \alpha_0$. These profiles are depicted as the solid lines in the three panels in Figure 8. Focusing only on these profiles, we see that, as expected, 10 au (being the innermost gap) is the most efficient

barrier relative to the other gap locations (left panel). However, it remains just as efficient a barrier as when paired with one or more outer gaps (middle and right panels). This implies that irrespective of whether additional outer gaps exist, a deep inner disk gap can be an excellent barrier to pebble delivery. In a similar vein, the 40 au gap is just as efficient a barrier whether present alone or when paired with an even outer 70 au gap. For the disk with three gaps, the additional presence of a third gap at 70 au (that would block the least amount of icy pebble material from the inner disk), even if it is deep, does not matter at all.

We next consider what would happen if an inner gap is shallower in depth compared to the outer gaps in the disk. We assume a gap depth of $1.5 \times \alpha_0$ for only the innermost 10 au gap, and retain the fiducial gap depth for the outer two gaps. Profiles incorporating a shallow 10 au gap are depicted with a dotted-dashed profile in the same three panels of Figure 8. The left panel shows how a shallow 10 au gap is inefficient at trapping particles beyond it and continuously leaks material through the gap (as seen earlier in Section 3.3). When paired with an outer deep gap, the outer gap is able to restrict pebble delivery from beyond it, and thus reduces the total amount of material that may be leaked through the inner shallow gap. Here, as expected, the 40 au gap performs better than the 70 au gap simply because it has more material to block compared to the latter. Even here, in the case of the disk simulation with three gaps, the additional presence of a third gap at 70 au does not matter at all. Another case with two shallow inner gaps at 10 and 40 au, accompanying a deep outer gap at 70 au, shows a slightly more prolonged vapor enrichment (little over 1 Myr) in the inner disk.

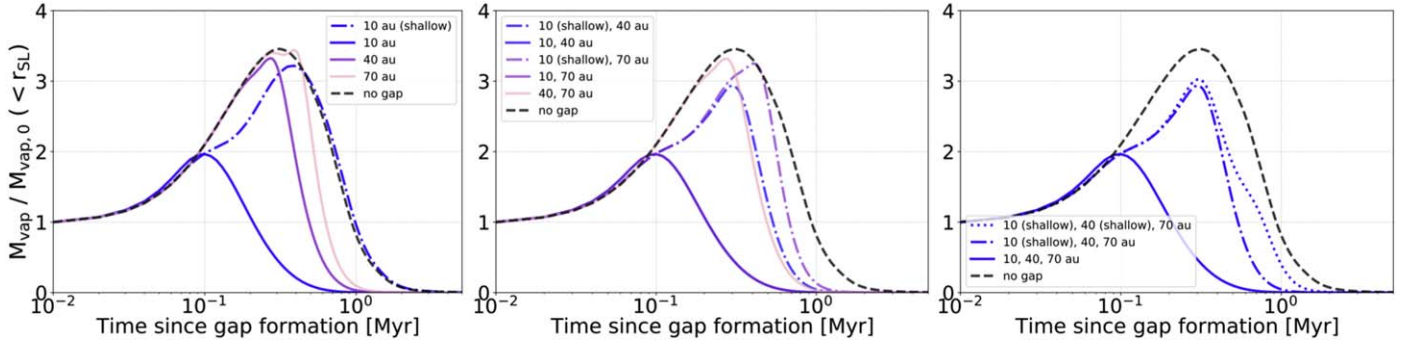


Figure 8. Time evolution of vapor enrichment for simulations with one gap (left panel), two gaps (middle panel), and three gaps (right panel) with fiducial $v_f = 5 \text{ m s}^{-1}$ both inside and outside of the snow line, and with planetesimal formation. Colors denote specific gap locations; solid colored lines denote deep gaps at those locations, while dotted–dashed colored lines denote shallow gap(s) at those locations. The dotted line in right panel denotes the case with two shallow interior gaps, along with a deep outer gap. The black dashed line shows the no-gap case for comparison, in each panel.

All these simulations suggest that water delivery to the inner disk is strongly regulated by the deepest innermost gap that is present, or in combination with the pair of deep innermost gaps that is present.

4. Discussion

In the following section, we discuss the main insights gained from the parameter study described in detail in Section 3.

4.1. Disk Structure and Vapor Enrichment

The overarching motivation of this work is to understand how the outer disk may affect vapor enrichment in the inner disk by altering the pebble dynamics in the outer disk. Disk structure present in the form of a gap (which is the focus of this work) can block partially or completely the passage of radially drifting ice-rich material across it, which otherwise unhindered in its inward travel would sublimate to vapor in the inner disk within the snow line. In this work, we perform several simulations where we vary the radial location of the gap, the depth of the gap (i.e., how efficiently it can filter out particles from passing through it), and even explore the influence of additional gaps on inner disk vapor enrichment. For our fiducial value of fragmentation velocity $v_f = 5 \text{ m s}^{-1}$ (representing some median value from all experimental results performed so far on the tensile strengths of icy and silicate particles against collisions), and for a turbulent viscosity $\alpha = 1 \times 10^{-3}$, we find that for a uniform disk, the inner regions can become strongly enriched in water vapor due to the delivery of ice-rich pebbles from the outer disk. This enrichment can generally last for about 1 Myr or so, and has a typical profile: an increase with pebble delivery, a peak (when bulk pebble mass is delivered), and subsequent decrease with stellar accretion. For a disk with a gap, vapor enrichment may be less strong, with lower peak enrichment as compared to the initial value for a uniform disk with no gap; vapor enrichment episodes may also be more time limited for disks with a gap, compared to disks with no gap. If all gaps are deep and are efficient barriers against pebble passage, then gaps present in the outer disk (~ 50 – 100 au) have the disadvantage that they can only block as much material as there is beyond them. An inner gap (~ 10 au) in this way occupies a special location in the disk, simply because it is able to block most of the amount of ice-rich material originating from the outer disk, which would drift inwards into the inner disk.

Gaps may not be always efficient at trapping material beyond it. The depth of the gap affects its trapping efficiency. We find that, just as before, it is the depth of the innermost gap that regulates the vapor enrichment in the inner disk. A shallow inner gap can continuously leak material from beyond it, resulting in a longer and higher vapor enrichment episode in the inner disk than with a deep inner gap. Shallow outer gaps would have this effect as well, though not as strongly, as they do not block enough ice beyond them.

For the above reasons, if there are any additional gaps that accompany an inner gap in the disk, their presence has no real effect unless the inner gaps themselves are shallow therefore making for weak traps. If that is the case, then it is the best combination of inner gaps (that together effectively trap more pebble mass) that regulates pebble delivery into the inner disk, as discussed in Section 3.8.

Overall, we find that it is the innermost gaps that have a dominating influence in dictating pebble delivery and therefore water enrichment in the inner disk.

4.2. Disk Structure versus Planetesimal Formation

The formation of a gap and the trapping of dust material beyond it, although extremely efficient, may not be the only way to block pebble delivery into the inner disk. As explored in other studies (McClure 2019), it is also possible that planetesimal formation may be able to lock volatile-rich material within planetesimals and prevent them from entering the inner disk. Najita et al. (2013) also theorized that the locking up of water ice in planetesimals could be a possible reason why they found a correlation between HCN/ H_2O ratios and dust disk mass; more massive disks may have more planetesimal formation, and therefore lock more water ice in them, leading to a lower relative abundance of H_2O compared to HCN in the inner regions of those disks. In this study, we include planetesimal formation in one set of simulations to understand which of the two effects (the presence of gaps or planetesimal formation) may have the more dominant impact on vapor enrichment in the inner disk. We find that for $v_f = 5$ or 10 m s^{-1} , gaps have a stronger effect than planetesimal formation. When $v_f \leq 10 \text{ m s}^{-1}$, particle sizes are still limited by the fragmentation limit such that planetesimal formation mainly only takes place in the pressure bump beyond the gap. However, for $v_f = 15 \text{ m s}^{-1}$, particles grow to sizes large enough that a significant mass of planetesimals begins to form just beyond the snow line as well. This additional surge of

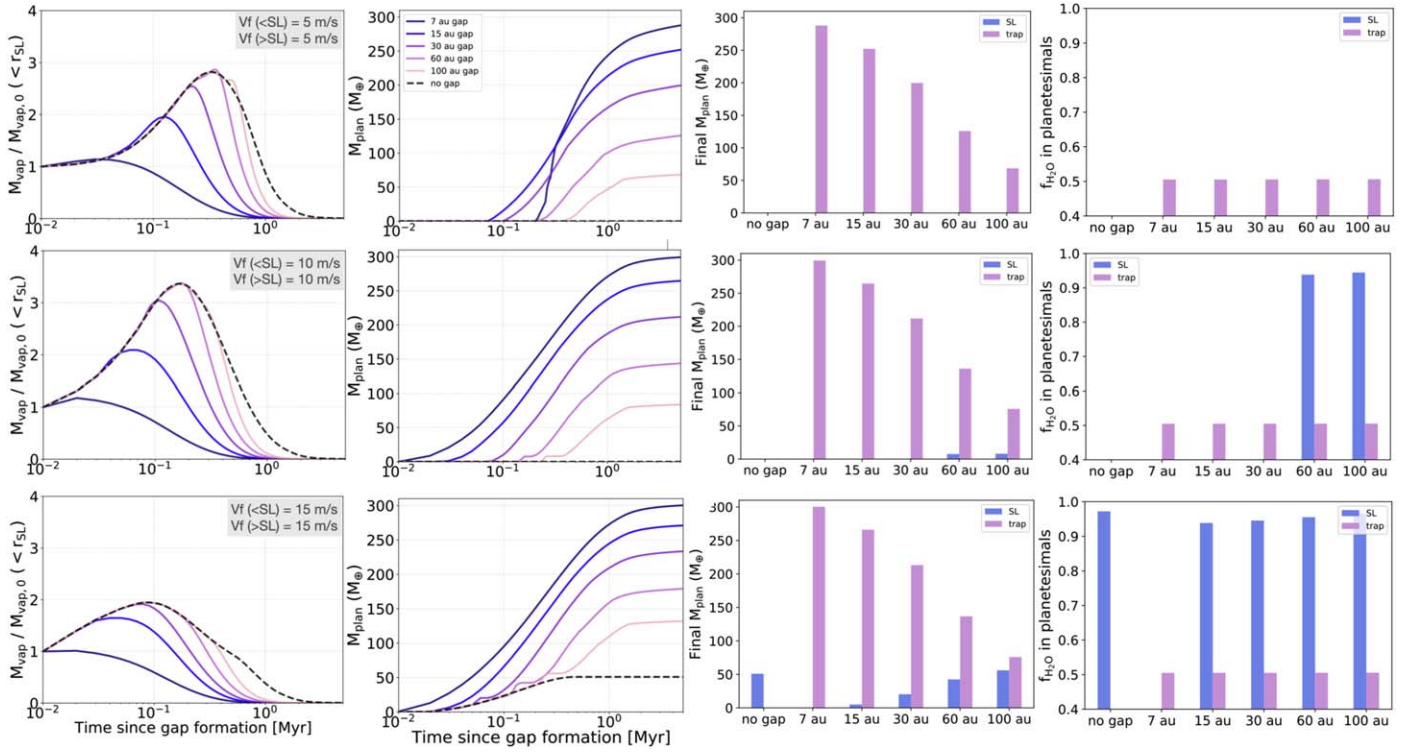


Figure 9. Plots shown are similar to Figure 7, but with a higher initial disk mass of $M_{\text{disk}} = 0.1 M_{\odot}$.

planetesimal formation locks water ice beyond the snow line and prevents its delivery into the inner disk, drastically depleting the water content in the inner disk. Thus, we see that it is only for very high values of v_f ($\sim 15 \text{ m s}^{-1}$) that planetesimal formation starts to become a dominating influence on vapor enrichment. For a more reasonable range of v_f values, pebble trapping by gap formation may still be the most efficient way to block pebble delivery into the inner disk. We perform the same simulations presented in Figure 7 for a higher initial disk mass ($M_{\text{disk}} = 0.1 M_{\odot}$) shown in Figure 9. We find no clear trend with increasing disk mass for $v_f = 5, 10,$ and 15 m s^{-1} . Our simulations thus lead us to conclude that even at a higher initial disk mass, pebble delivery into the inner disk is primarily affected by trapping beyond gaps rather than planetesimal formation (see also Appendix D, Figure 15).

4.3. Fragmentation Velocity versus Turbulent Viscosity

The fragmentation velocity v_f is an important physical quantity that dictates how large particles can get before breaking apart from collisions and is determined experimentally from microgravity experiments on dust aggregates. A high v_f can enable the growth of a sufficient mass of pebbles that can eventually participate in planetesimal and planet formation, while a low v_f can severely restrict the growth of particles to submillimeter sizes, which may be too small to contribute to planet formation. Recent experiments suggest a lack of consensus on the relative tensile strength of icy dust aggregates compared to bare silicates (Musioliik et al. 2016; Gundlach et al. 2018; Musioliik & Wurm 2019). In our work, we considered both possibilities that experiments yield: either that icy silicates are stickier than bare silicates and therefore have a higher v_f threshold, or that both are equally susceptible to collisions and have comparable v_f . We therefore performed several simulations considering a range of v_f . The maximum

particle size at the fragmentation limit a_{frag} is proportional to v_f^2/α (Equation (9)). We therefore expanded our suite of simulations to include a range of α values.

Due to the dependence on v_f^2/α , we find that our results fall into three general categories:

1. *Low α .* This category (top row) represents our typical simulations, showing a peak enrichment period in vapor that eventually declines with time in the inner disk at around a megayear or so for the low v_f case (1 m s^{-1}), and around 0.5 Myr for the high v_f case ($\geq 5 \text{ m s}^{-1}$). Disks with low turbulence show different extents of vapor enrichment in the inner disk depending on whether a gap is present in the outer disk, and on the radial location of the gap.
2. *Moderate α .* This category (second and third rows) shows mixed outcomes. For α ranging from $\sim 5 \times 10^{-4}$ to 1×10^{-3} , for low v_f (1 m s^{-1}), the vapor mass slowly declines in the inner disk with time. (Note, for $\sim 5 \times 10^{-4}$, the vapor mass stays roughly constant for a disk with no gap.) On the other hand, the high v_f ($\geq 5 \text{ m s}^{-1}$) simulations follow the profiles in category 1, where as discussed above, the inner disk is temporarily enriched in vapor. The extent of peak enrichment is dependent on α (i.e., higher α leads to lower peak enrichment) and whether there is a gap in the disk, and if present, where.
3. *High α .* This category (bottom row) shows only a decline in the mass of vapor with time over 5 Myr, with no period of enrichment like in the other cases. For higher v_f (10 m s^{-1}), cases with a gap show an earlier depletion of vapor within ~ 1 Myr after gap formation.

In general, if most disks are truly less turbulent than previously thought, as recent observations suggest (Pinte et al. 2016; Flaherty et al. 2020; Rosotti 2023), then irrespective of v_f , our simulations suggest that the inner disk will experience an intense but short-

lived episode of vapor enrichment, with the presence and location of the gap determining the intensity of the enrichment episode. On the other hand, disks with high turbulent α , irrespective of v_f , may not see any enrichment in vapor in the inner regions. In this way, vapor enrichment can be a diagnostic of turbulence in the disk, although a time-evolving one.

4.4. Origin of Compact Disks

Recent studies (Kurtovic et al. 2021; Jennings et al. 2022) suggest that substructure may be common in compact disks. Compact dust disks may form from rapid dust evolution and drift from previously large disks that perhaps did not have any major substructure that hindered pebble drift (van der Marel & Mulders 2021). As discussed in detail in this study, such unstructured uniform disks likely show strong and prolonged vapor enrichment lasting ~ 1 Myr in their inner disks. It is, however, also possible that some disks are simply born smaller in size (Najita & Bergin 2018). For all the simulations presented in this work, we choose the initial size of the gaseous disk to be 500 au (with a critical radius of 70 au, concentrating most of the disk mass within), and do not actually model small disks. However, we still attempt to predict vapor enrichment outcomes for disks that formed small, based on our study.

The initial disk mass that would have to be assumed for modeling small disks is important. If we adopt a similar initial disk mass ($\sim 0.05 M_\odot$) as we did for disks in this study, these small disks would be highly dense. Any gaps in such a disk would be shallower and therefore even more “leaky,” and would allow for much more high and prolonged vapor enrichment in its inner regions. If we rather adopt an initial disk mass that is presumably scaled to its disk size, such a disk would be a small-scale version of the disks presented here, and would likely exhibit similar but smaller vapor enrichment profiles, as discussed in detail in this work, i.e., deep inner gaps in these disks can efficiently block pebble delivery (leading to low vapor enrichment) but shallow gaps may not (leading to moderate vapor enrichment). Thus, while small uniform disks may show high and prolonged vapor enrichment if born large, we argue that even if born small, there is a possibility that small disks with inner gaps may also show high and prolonged vapor enrichment if they formed dense.

5. Summary and Conclusions

In this study, we aimed to understand the overall effect of disk structure on vapor enrichment in the inner disk, and determine what physical properties had most influence on the extent of enrichment. We built on our previous modeling (Kalyaan et al. 2021) and employed a multimillion-year disk evolution model that incorporated the two-population model of Birnstiel et al. (2012) and included volatile transport, considering the sublimation of ice and freeze-out of vapor on solids at the snow line. Furthermore, we also included disk structure in the form of gaps that are able to trap icy pebbles and dust particles beyond them and explored in detail the effect of the presence of gaps, their radial location, and depth on the vapor enrichment in the inner disk. We finally also explored the effect of planetesimal formation. We present the main highlights of our study as follows:

1. The time evolution of the mass of vapor in the inner disk depends on the fragmentation velocity v_f of dust particles and turbulent viscosity α in the disk.
2. If disks are not very turbulent, i.e., $\alpha \leq 5 \times 10^{-4}$, then our simulations suggest that they likely experience a strong and prolonged episode of vapor enrichment (lasting about 1 Myr) followed by the depletion of vapor from the inner disk. Furthermore, the presence of a gap can significantly alter the extent of vapor enrichment, especially if present closer to the star (~ 7 au or 15 au).
3. More turbulent disks, on the other hand, may only see a constant depletion in water vapor content in the inner disk, irrespective of v_f ; the presence of a gap or its location does not make much of a difference.
4. Shallow gaps may continuously leak material, continuously enriching the inner disk with vapor. Ultimately, vapor enrichment is regulated by the deepest innermost gap present, or if multiple gaps are present, the pair of inner gaps that together trap the most dust mass.
5. For a reasonable range in v_f ($\leq 10 \text{ m s}^{-1}$), locking up ices in forming planetesimals beyond the snow line does not appear to have as much of an impact as the presence of gaps does in regulating vapor enrichment in the inner disk.
6. For $v_f \geq 10 \text{ m s}^{-1}$, planetesimal formation occurs in a few distinct locations in disks—either beyond the snow line or in dust traps beyond gaps, if gaps are present. Planetesimals that formed via the cold-finger effect at the snow line are much more ice-rich (up to ice-to-rock ratios of 0.9 in our simulations) than planetesimals that formed at the snow line (~ 0.5).
7. Inner disk vapor abundance can be an important proxy for pebble mass fluxes into the terrestrial planet-forming region. Although sensitive to v_f and α , smooth disks without structure may lead to more inner disk planet formation.

Acknowledgments

We thank the anonymous reviewer for helpful suggestions that improved the manuscript. A.K. and A.B. acknowledge support from NASA/Space Telescope Science Institute grant No. JWST-GO-01640. Support for F.L. was provided by NASA through the NASA Hubble Fellowship grant No. HST-HF2-51512.001-A awarded by the Space Telescope Science Institute, which is operated by the Association of Universities for Research in Astronomy, Incorporated, under NASA contract NAS5-26555. G.D.M. acknowledges support from FONDECYT project 11221206, from ANID—Millennium Science Initiative—ICN12_009, and the ANID BASAL project FB210003. M.L. acknowledges funding from the European Research Council (ERC Starting Grant 101041466-EXO-DOSS). G.R. acknowledges funding by the European Union (ERC Starting Grant DiscEvol, project number 101039651). Views and opinions expressed are however those of the author (s) only and do not necessarily reflect those of the European Union or the European Research Council Executive Agency. Neither the European Union nor the granting authority can be held responsible for them.

Appendix A

Gas Accretion versus Vapor Diffusion

In addition to the “vapor abundance” plots we show in Figures 2 and 3, we present the same plots for simulations with v_f of 1 and 10 m s^{-1} (for fiducial α) in Figures 10 and 11 to illustrate the relative rates of gas and vapor transport in the inner disk. The mass of gas within the snow line region

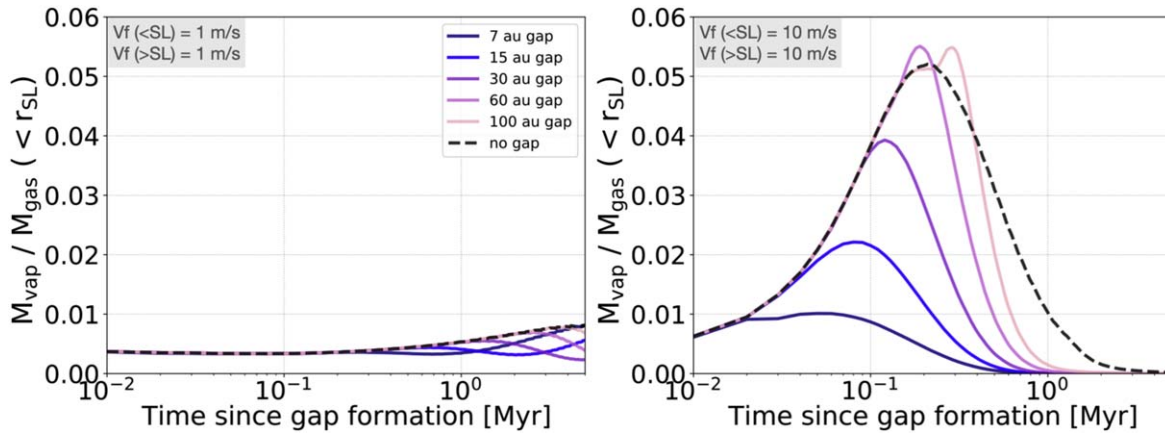


Figure 10. Plots showing “vapor abundance,” i.e., the ratio of the mass of vapor within the snow line to the mass of bulk gas within the snow line, for simulations with a radially uniform fragmentation velocity $v_f = 1 \text{ m s}^{-1}$ (left) and 10 m s^{-1} (right). Lines and colors are as in Figure 2.

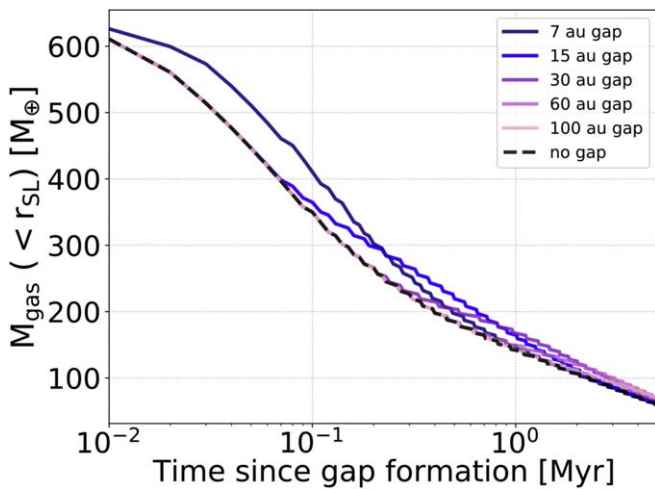


Figure 11. Plot showing the mass of gas present within the snow line over time for typical simulations with a fiducial initial disk mass. Note that the snow line moves slightly inward with time.

monotonically decreases with time as it is mainly accreted onto the star. In addition, water vapor is a trace species that advects and diffuses throughout the bulk gas. Generated at the snow line by drifting icy particles, vapor can diffuse inward and be accreted onto the star, or “retro-diffuse” again across the snow line. For 1 m s^{-1} , our simulations show that until about 0.3 Myr, both gas and residual vapor in the inner disk are accreted onto the star at the same rate. When pebbles start to drift inward of the snow line from 0.3 Myr until 5 Myr, the inner disk gradually gets more vapor rich, if no gap is present. If a gap is present for this case, as well as for larger v_f (5 or 10 m s^{-1}), the inner disk is quickly flooded with vapor (from the incoming icy pebble population), which subsequently diffuses out of the region (via the star or snow line) slightly more rapidly than stellar accretion.

Appendix B Gap Depth

In this section, we analyze two simulations performed with different gap depths in some more detail. In Figures 12 and 13, we show two simulations of the 7 au gap with low ($1.5 \times \alpha_0$) and fiducial gap depths ($10 \times \alpha_0$). Figure 12 shows the time evolution of the surface density of large and small particles ($0.1 \mu\text{m}$) at the snow line region and the dust trap; large and small particles here correspond to the two populations in Birnstiel et al. (2012) used in this work. In Figure 13, we show $\Sigma(a, r)$ contour plots at two specific snapshots in time (0.06 and 0.4 Myr) for the same simulations, which we generate using the reconstruction scheme developed in Birnstiel et al. (2015). This work broadly demarcates the particle size—radial distance parameter space into regions where the fragmentation, drift, or turbulent diffusion of particles is efficient. They employ a semi-analytical treatment from which they compute a surface density for all particle size bins at each radial distance r from the two-population model, effectively “reconstructing” the full dust evolution simulations from Birnstiel et al. (2010). We assume that a gap being a local perturbation would not significantly affect where the global processes of the fragmentation, growth, and drift of dust particles across the disk are dominant. The top-right panel in Figure 12 shows that for a low gap depth of $1.5 \times \alpha_0$, few particles are trapped and only temporarily in the pressure bump beyond the gap. Dust material is instead continuously leaking out of the trap and seen surging around 0.4 Myr at the snow line (top-left panel), which eventually shows up as water vapor (Figure 4) within the snow line. Top panels in 13 confirm this poor trapping by showing high density of large millimeter- to centimeter-sized particles in the inner disk that have accumulated and grown at 0.4 Myr, compared to the very low density of such particles beyond the gap. On the contrary, for a gap depth of $10 \times \alpha_0$, large and small particles accumulate, grow, and are trapped well for several million years beyond the gap in the pressure bump (lower right panel of Figure 12). The inner disk is consequently depleted at 0.4 Myr as seen in the lower right panels of Figures 12 and 13.

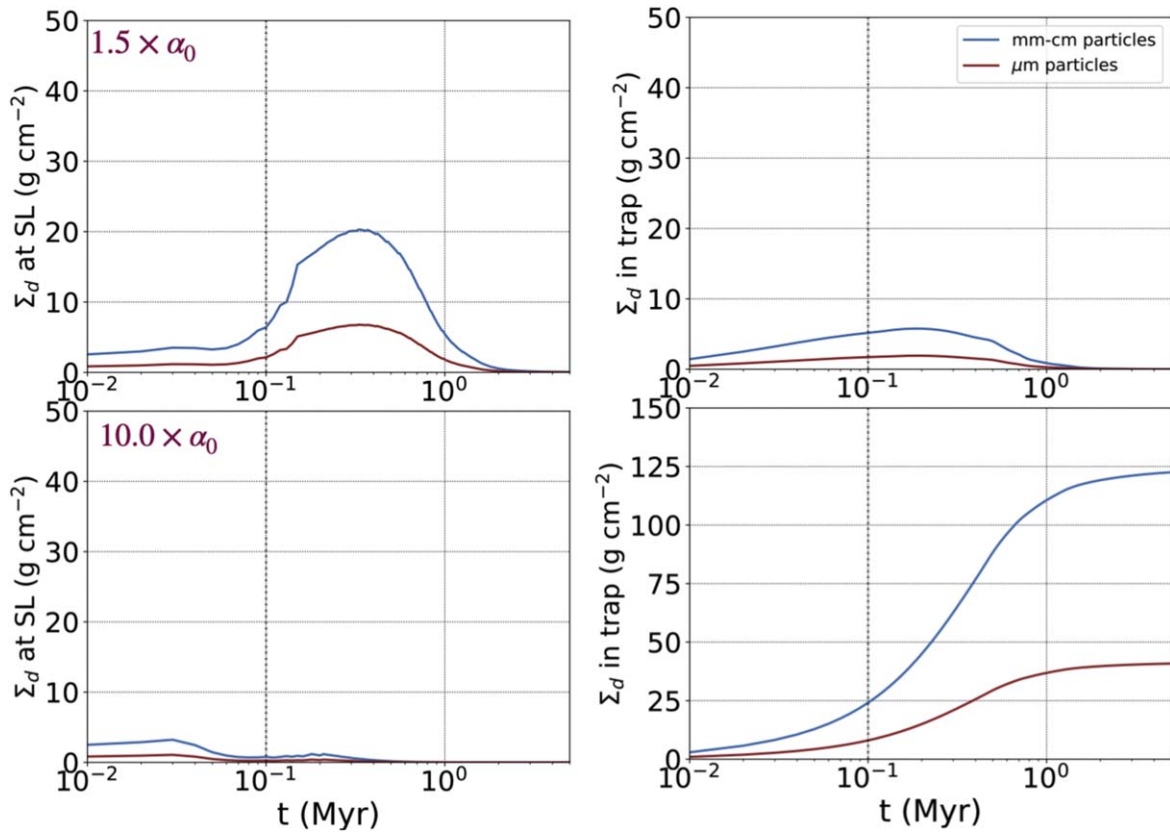


Figure 12. Dust surface densities for large (blue lines) and small particles (brown lines) at the snow line (left column) and at traps (right column) for two simulations of different gap depths for a gap at 7 au. The top row shows a simulation with a gap depth of $1.5 \times \alpha_0$; the bottom row shows a simulation with a gap depth of $10 \times \alpha_0$.

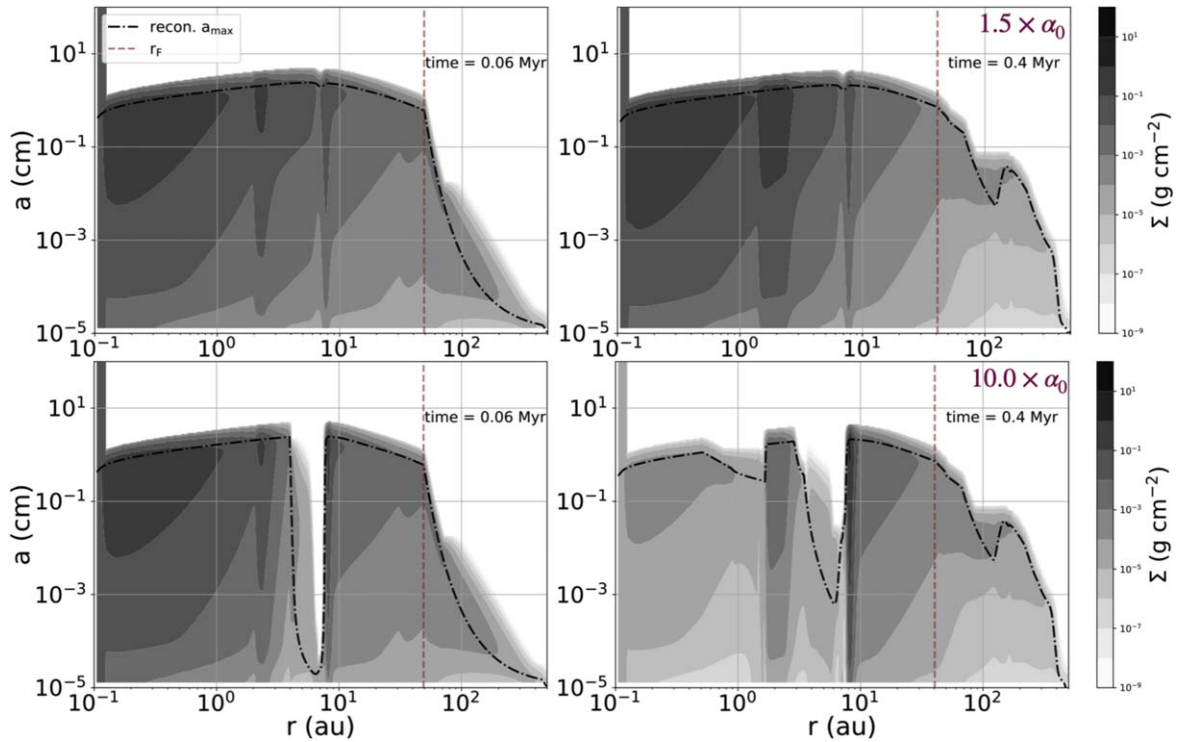


Figure 13. Dust density distributions for the same simulations depicted in Figure 12 at two different snapshots in time: at 0.06 Myr (left column) and at 0.4 Myr (right column). Rows show simulations with a shallower gap (top) or a deeper gap (bottom). The black dashed line shows the maximum particle size $a_{\text{max}}(r)$ as computed by the reconstruction model of Birnstiel et al. (2015); the vertical brown dashed line shows the fragmentation radius, r_f , representing the radial extent of the fragmentation-dominated region in disks, also computed by the same model.

Appendix C Leaky Gaps

In Kalyaan et al. (2021; see their Appendix B and Figure 12), we show how effective different gaps are in trapping particles of different sizes beyond them. As we mentioned before in Section 3.2, with increasing radial distance, pressure bumps are able to trap smaller and smaller particles. Therefore, for the same particle size, a similar gap would be leakier in the inner disk than in the outer disk.

This also holds if we include the growth and fragmentation of particles. We show similar plots of the trapping efficiency of gaps based on their radial location in Figure 14. For our fiducial gap depth of $\alpha = 10 \times \alpha_0$, we find that the innermost gaps (e.g., gap at 7 au) are slightly “leaky,” as compared to outer gaps. The gap at 7 au allows the passage of small particles that are otherwise efficiently trapped beyond gaps at larger radii (see also Stammler et al. 2023).

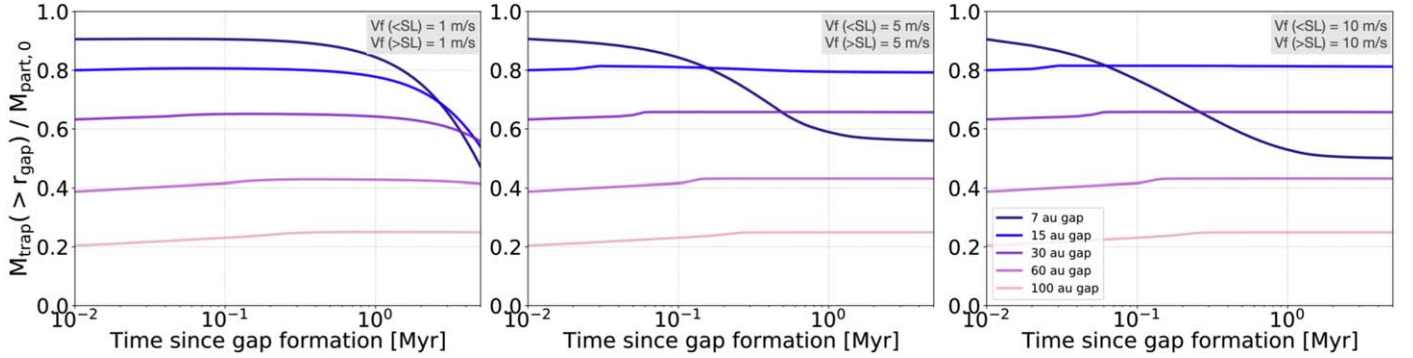


Figure 14. Plots showing the fraction of the total initial pebble mass trapped beyond the gap at each time for simulations with $v_{\text{frag}} = 1 \text{ m s}^{-1}$ (left), 5 m s^{-1} (middle), and 10 m s^{-1} (right).

Appendix D Planetesimal Formation over Time

In addition to Figures 7 and 9, we show separately the masses of planetesimals that form either at the snow line or at the dust trap beyond the gap in Figure 15. Generally,

planetesimal formation proceeds at the dust trap for a longer duration. On the other hand, the snow line region may only experience a short “burst” of planetesimal formation. Doubling the initial disk mass does not significantly affect the duration of planetesimal formation at either location.

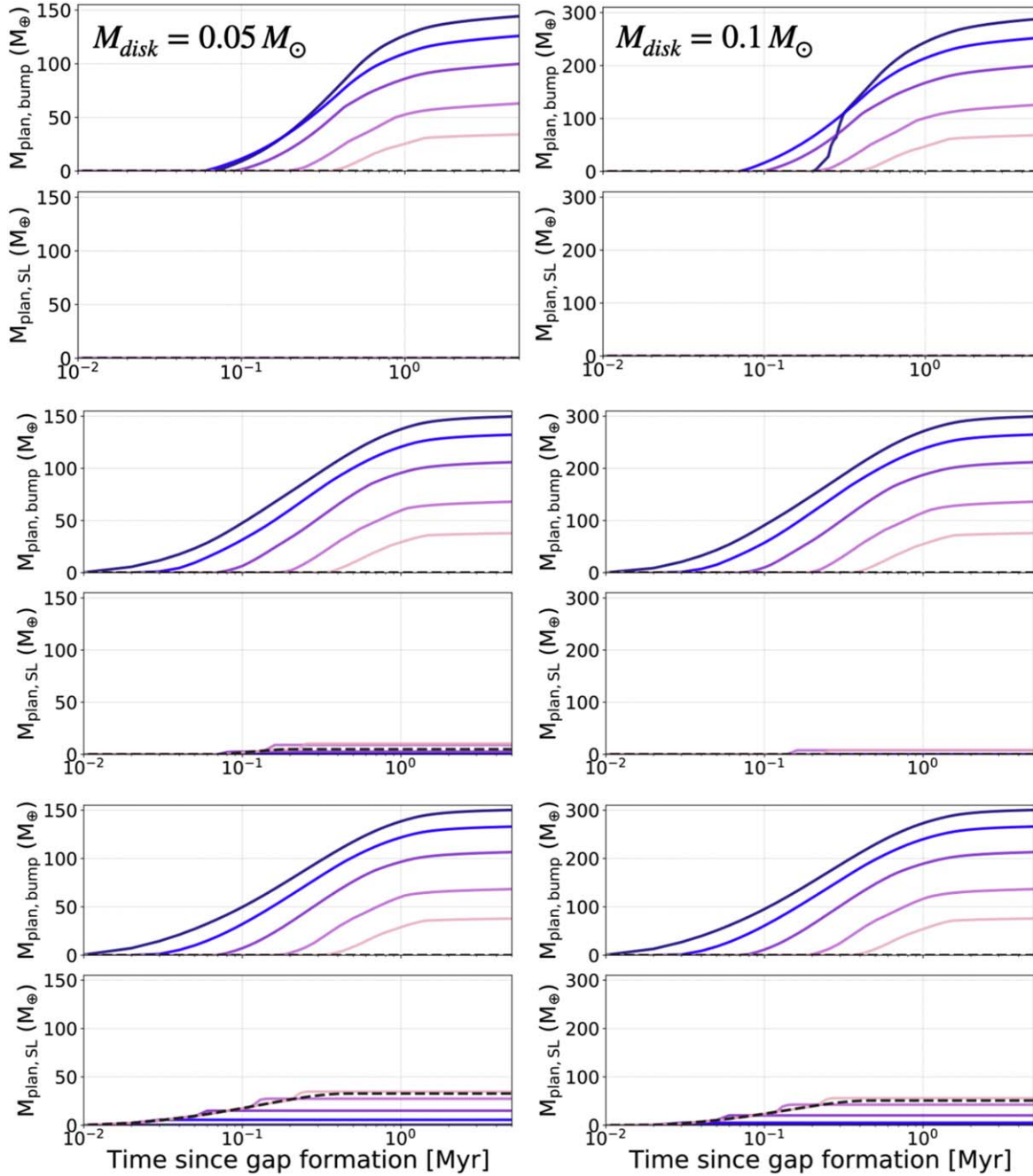











Figure 15. Figures showing the mass of planetesimals formed over time at either the water snow line or dust trap (pressure bump) beyond the gap, when planetesimal formation is included. The left column shows simulations with a fiducial disk mass; the right column shows higher disk masses. The top, middle, and bottom rows represent $v_{\text{frag}} = 5, 10, \text{ and } 15 \text{ m s}^{-1}$, respectively. In each case, planetesimal formation takes place for a limited duration, after which the mass of planetesimals formed remains constant with time.

ORCID iDs

Anusha Kalyaan  <https://orcid.org/0000-0002-5067-1641>
 Paola Pinilla  <https://orcid.org/0000-0001-8764-1780>
 Sebastiaan Krijt  <https://orcid.org/0000-0002-3291-6887>
 Andrea Banzatti  <https://orcid.org/0000-0003-4335-0900>
 Giovanni Rosotti  <https://orcid.org/0000-0003-4853-5736>
 Gijs D. Mulders  <https://orcid.org/0000-0002-1078-9493>
 Michiel Lambrechts  <https://orcid.org/0000-0001-9321-5198>
 Feng Long  <https://orcid.org/0000-0002-7607-719X>
 Gregory J. Herczeg  <https://orcid.org/0000-0002-7154-6065>

References

- Andama, G., Ndugu, N., Anguma, S. K., & Jurua, E. 2022, *MNRAS*, **512**, 5278
- Andrews, S. M. 2020, *ARA&A*, **58**, 483
- Appelgren, J., Lambrechts, M., & Johansen, A. 2020, *A&A*, **638**, A156
- Ataiee, S., Pinilla, P., Zsom, A., et al. 2013, *A&A*, **553**, L3
- Bae, J., Zhu, Z., Baruteau, C., et al. 2019, *ApJL*, **884**, L41
- Bai, X.-N., & Stone, J. M. 2010, *ApJ*, **722**, 1437
- Banzatti, A., Pascucci, I., Bosman, A. D., et al. 2020, *ApJ*, **903**, 124
- Birnstiel, T., Andrews, S. M., Pinilla, P., & Kama, M. 2015, *ApJL*, **813**, L14
- Birnstiel, T., Dullemond, C. P., & Brauer, F. 2010, *A&A*, **513**, A79
- Birnstiel, T., Klahr, H., & Ercolano, B. 2012, *A&A*, **539**, A148
- Blum, J., & Wurm, G. 2000, *Icar*, **143**, 138
- Booth, R. A., Clarke, C. J., Madhusudhan, N., & Ilee, J. D. 2017, *MNRAS*, **469**, 3994
- Carrera, D., & Simon, J. B. 2022, *ApJL*, **933**, L10
- Carrera, D., Simon, J. B., Li, R., Kretke, K. A., & Klahr, H. 2021, *AJ*, **161**, 96
- Ciesla, F. J., & Cuzzi, J. N. 2006, *Icar*, **181**, 178
- Cuzzi, J. N., & Zahnle, K. J. 2004, *ApJ*, **614**, 490
- Drażkowska, J., & Alibert, Y. 2017, *A&A*, **608**, A92
- Drażkowska, J., Alibert, Y., & Moore, B. 2016, *A&A*, **594**, A105
- Flaherty, K., Hughes, A. M., Simon, J. B., et al. 2020, *ApJ*, **895**, 109
- Gundlach, B., & Blum, J. 2015, *ApJ*, **798**, 34
- Gundlach, B., Schmidt, K. P., Kreuzig, C., et al. 2018, *MNRAS*, **479**, 1273
- Güttler, C., Blum, J., Zsom, A., Ormel, C. W., & Dullemond, C. P. 2010, *A&A*, **513**, A56
- Hartmann, L., Calvet, N., Gullbring, E., & D'Alessio, P. 1998, *ApJ*, **495**, 385
- Huang, J., Andrews, S. M., Dullemond, C. P., et al. 2018, *ApJL*, **869**, L42
- Jennings, J., Tazzari, M., Clarke, C. J., Booth, R. A., & Rosotti, G. P. 2022, *MNRAS*, **514**, 6053
- Kalyaan, A., & Desch, S. J. 2019, *ApJ*, **875**, 43
- Kalyaan, A., Pinilla, P., Krijt, S., Mulders, G. D., & Banzatti, A. 2021, *ApJ*, **921**, 84
- Kley, W., & Dirksen, G. 2006, *A&A*, **447**, 369
- Kurtovic, N. T., Pinilla, P., Long, F., et al. 2021, *A&A*, **645**, A139
- Lambrechts, M., Morbidelli, A., Jacobson, S. A., et al. 2019, *A&A*, **627**, A83
- Li, R., & Youdin, A. N. 2021, *ApJ*, **919**, 107
- Lichtenberg, T., Drażkowska, J., Schönbachler, M., Golabek, G. J., & Hands, T. O. 2021, *Sci*, **371**, 365
- Long, F., Herczeg, G. J., Harsono, D., et al. 2019, *ApJ*, **882**, 49
- Long, F., Pinilla, P., Herczeg, G. J., et al. 2018, *ApJ*, **869**, 17
- Lynden-Bell, D., & Pringle, J. E. 1974, *MNRAS*, **168**, 603
- Marzari, F., & D'Angelo, G. 2020, *A&A*, **641**, A125
- Marzari, F., D'Angelo, G., & Picogna, G. 2019, *AJ*, **157**, 45
- McClure, M. K. 2019, *A&A*, **632**, A32
- Morbidelli, A., Bitsch, B., Crida, A., et al. 2016, *Icar*, **267**, 368
- Mousis, O., Aguichine, A., Bouquet, A., et al. 2021, *PSJ*, **2**, 72
- Musiolik, G., Teiser, J., Jankowski, T., & Wurm, G. 2016, *ApJ*, **827**, 63
- Musiolik, G., & Wurm, G. 2019, *ApJ*, **873**, 58
- Najita, J. R., & Bergin, E. A. 2018, *ApJ*, **864**, 168
- Najita, J. R., Carr, J. S., Pontoppidan, K. M., et al. 2013, *ApJ*, **766**, 134
- Öberg, K. I., & Bergin, E. A. 2021, *PhR*, **893**, 1
- Paardekooper, S. J., & Mellema, G. 2006, *A&A*, **453**, 1129
- Pinilla, P., Benisty, M., & Birnstiel, T. 2012, *A&A*, **545**, A81
- Pinilla, P., Benisty, M., Birnstiel, T., et al. 2014, *A&A*, **564**, A51
- Pinte, C., Dent, W. R. F., Ménard, F., et al. 2016, *ApJ*, **816**, 25
- Pontoppidan, K. M., Salyk, C., Bergin, E. A., et al. 2014, in *Protostars and Planets VI*, ed. H. Beuther et al. (Tucson, AZ: Univ. Arizona Press), 363
- Rice, W. K. M., Armitage, P. J., Wood, K., & Lodato, G. 2006, *MNRAS*, **373**, 1619
- Ros, K., & Johansen, A. 2013, *A&A*, **552**, A137
- Rosotti, G. P. 2023, *NewAR*, **96**, 101674
- Schneider, A. D., & Bitsch, B. 2021a, *A&A*, **654**, A72
- Schneider, A. D., & Bitsch, B. 2021b, *A&A*, **654**, A71
- Schoonenberg, D., & Ormel, C. W. 2017, *A&A*, **602**, A21
- Schoonenberg, D., Ormel, C. W., & Krijt, S. 2018, *A&A*, **620**, A134
- Stammler, S. M., Lichtenberg, T., Drażkowska, J., & Birnstiel, T. 2023, *A&A*, **670**, L5
- Stevenson, D. J., & Lunine, J. I. 1988, *Icar*, **75**, 146
- Teague, R., Bae, J., Bergin, E. A., Birnstiel, T., & Foreman-Mackey, D. 2018, *ApJL*, **860**, L12
- Teyssandier, J., & Ogilvie, G. I. 2017, *MNRAS*, **467**, 4577
- Toci, C., Rosotti, G., Lodato, G., Testi, L., & Trapman, L. 2021, *MNRAS*, **507**, 818
- van der Marel, N., & Mulders, G. D. 2021, *AJ*, **162**, 28
- Venturini, J., Ronco, M. P., & Guilera, O. M. 2020, *SSRv*, **216**, 86
- Wölfer, L., Facchini, S., van der Marel, N., et al. 2023, *A&A*, **670**, A154
- Zhang, K., Booth, A. S., Law, C. J., et al. 2021, *ApJS*, **257**, 5
- Zhang, S., Zhu, Z., Huang, J., et al. 2018, *ApJL*, **869**, L47
- Zhu, Z., Nelson, R. P., Dong, R., Espaillat, C., & Hartmann, L. 2012, *ApJ*, **755**, 6
- Zsom, A., Sándor, Z., & Dullemond, C. P. 2011, *A&A*, **527**, A10